

1 **Examination of aerosol impacts on convective clouds and precipitation in two  
2 metropolitan areas in East Asia; how varying depths of convective clouds between  
3 the areas diversify those aerosol effects?**

4

5 Seoung Soo Lee<sup>1,2</sup>, Jinho Choi<sup>3</sup>, Goun Kim<sup>4</sup>, Kyung-Ja Ha<sup>2,5,6</sup>, Kyong-Hwan Seo<sup>3</sup>, Chang-

6 Hoon Jung<sup>7</sup>, Junshik Um<sup>3</sup>, Yutong Zheng<sup>8</sup>, Jianping Guo<sup>9</sup>, Sang-Keun Song<sup>10</sup>

Formatted: Superscript

7

8 <sup>1</sup>Earth System Science Interdisciplinary Center, University of Maryland, Maryland

9 <sup>2</sup>Research Center for Climate Sciences, Pusan National University, Busan, Republic of  
10 Korea

11 <sup>3</sup>Department of Atmospheric Sciences, Division of Earth Environmental System, Pusan  
12 National University, Busan, Republic of Korea

13 <sup>4</sup>Marine Disaster Research Center, Korea Institute of Ocean Science and Technology,  
14 Pusan, Republic of Korea

15 <sup>5</sup>Center for Climate Physics, Institute for Basic Science, Busan, Republic of Korea

16 <sup>6</sup>BK21 School of Earth and Environmental Systems, Pusan National University, Busan,  
17 Republic of Korea

18 <sup>7</sup>Department of Health Management, Kyungin Women's University, Incheon, Republic of  
19 Korea

20 <sup>8</sup>The Program in Atmospheric and Oceanic Sciences, Princeton University,  
21 and National Oceanic and Atmospheric Administration/Geophysical Fluid Dynamics  
22 Laboratory, Princeton, New Jersey, USA

23 <sup>9</sup>State Key Laboratory of Severe Weather, Chinese Academy of Meteorological Sciences,  
24 Beijing, China

25 <sup>10</sup>[Department of Earth and Marine Sciences, Jeju National University, Jeju, Republic of  
26 Korea](#)

**Formatted:** Font: (Asian) Times New Roman, Superscript

**Formatted:** Space Before: 0 pt, After: 0 pt, Line spacing: Double, Pattern: Clear

**Formatted:** Font: (Default) Times New Roman, (Asian) Times New Roman, 12 pt, Font color: Auto

**Formatted:** Font: (Default) Times New Roman, (Asian) Times New Roman, 12 pt, Not Italic, Font color: Auto

27

28 Corresponding author: Seoung Soo Lee

29 Office: (303) 497-6615

30 Fax: (303) 497-5318

31 E-mail: [cumulss@gmail.com](mailto:cumulss@gmail.com), [slee1247@umd.edu](mailto:slee1247@umd.edu)

32

33

34

35

36

37

38

39

40

41

42

43

44

45

46

47

48

49

50

51

52 **Abstract**

53

54 This study examines the role played by aerosols which act as cloud condensation nuclei  
55 (CCN) in the development of clouds and precipitation in two metropolitan areas in East  
56 Asia that have experienced substantial increases in aerosol concentrations over the last  
57 decades. These two areas are the Seoul and Beijing areas and the examination has been  
58 done by performing simulations using the Advanced Research Weather Research and  
59 Forecasting model as a cloud-system resolving model. CCN are advected from the  
60 continent to the Seoul area and this increases aerosol concentrations in the Seoul area.  
61 These increased CCN concentrations induce the enhancement of condensation that in turn  
62 induces the enhancement of deposition and precipitation amount in a system of less deep  
63 convective clouds as compared to those in the Beijing area. In a system of deeper clouds  
64 in the Beijing area, increasing CCN concentrations also enhance condensation but reduce  
65 deposition. This leads to CCN-induced negligible changes in precipitation amount. Also,  
66 in the system, there is a competition for convective energy among clouds with different  
67 condensation and updrafts. This competition results in different responses to increasing  
68 CCN concentrations among different types of precipitation, which are light, medium and  
69 heavy precipitation in the Beijing area. CCN-induced changes in freezing play a negligible  
70 role in CCN-precipitation interactions as compared to the role played by CCN-induced  
71 changes in condensation and deposition in both of the areas.

72

73

74

75

76

77

78

79

80

81

82

Deleted: ¶

86        **1. Introduction**

87

88        With increasing aerosol loading or concentrations, cloud-particle sizes can be changed. In  
89        general, with increasing droplet sizes, the efficiency of collision and collection among  
90        droplets increases. Increasing aerosol loading is known to make the droplet size smaller  
91        and thus make the efficiency of collision and collection among droplets lower. This leads  
92        to less droplets or cloud liquid forming raindrops and there is more cloud liquid present in  
93        the air to be evaporated or frozen. Studies have shown that increases in cloud-liquid mass  
94        due to increasing aerosol loading can enhance the freezing of cloud liquid and parcel  
95        buoyancy, which lead to the invigoration of convection (Rosenfeld et al., 2008; Fan et al.,  
96        2009). Via the invigoration of convection, precipitation can be enhanced. The dependence  
97        of aerosol-induced invigoration of convection and precipitation enhancement on aerosol-  
98        induced increases in condensational heating in the warm sector of a cloud system has been  
99        shown (e.g., van den Heever et al., 2006; Fan et al., 2009; Lee et al., 2018). Increasing  
100        cloud-liquid mass induces increasing evaporation, which intensifies gust fronts. This in  
101        turn strengthens convective clouds and increases the amount of precipitation (Khain et al.,  
102        2005; Tao et al., 2007; Storer et al., 2010; Tao et al., 2012; Lee et al., 2017; Lee et al.,  
103        2018). It is notable that aerosol-induced precipitation enhancement is strongly sensitive to  
104        cloud types that can be defined by cloud characteristics such as cloud depth (e.g., Tao et  
105        al., 2007; Lee et al., 2008; Fan et al., 2009).

Deleted:

106        Since East Asia was industrialized, there have been substantial increases in aerosol  
107        concentrations over the last decades in East Asia (e.g., Lee et al., 2013; Lu et al., 2011; Oh  
108        et al., 2015; Dong et al., 2019). These increases are far greater than those in other regions  
109        such as North America and Europe (e.g., Lu et al., 2011; Dong et al., 2019). While those  
110        increasing aerosols affect clouds, precipitation and hydrologic circulations in the  
111        continental East Asia, the increase in the advected aerosols from the continent to the  
112        Korean Peninsula affect clouds, precipitation and hydrologic circulations in the Korean  
113        Peninsula (Kar et al., 2009). This study aims to examine effects of the increasing aerosols,  
114        which particularly act as cloud condensation nuclei (CCN), and their advection on clouds  
115        and precipitation in East Asia. This study focuses on aerosols which act as CCN, but not  
116        ice-nucleating particles (INPs), to examine those effects, based on the fact that CCN

118 account for most of aerosol mass that affects clouds and precipitation, and CCN, but not  
119 INPs, are associated with above-described aerosol-induced invigoration of convection and  
120 intensification of gust fronts. Note that these aerosol-induced invigoration and  
121 intensification are two well-established major theories of aerosol-cloud interactions. As a  
122 first step to the examination, this study focuses on two metropolitan areas in East Asia  
123 which are the Beijing and Seoul areas. The population of each of the Beijing and Seoul  
124 areas is ~ 20 millions. Associated with this, these areas have lots of aerosol sources (e.g.,  
125 traffic) and have made a substantial contribution to the increases in aerosol concentrations  
126 in East Asia. Hence, we believe that these two cities can represent overall situations related  
127 to increasing aerosol concentrations in East Asia.

128 As mentioned above, aerosol-cloud interactions (and their impacts on precipitation) are  
129 strongly dependent on cloud types and thus to gain a more general understanding of those  
130 interactions, we select cases from the Beijing and Seoul areas with different cloud types.  
131 A selected case from the Beijing area involves deep convective clouds that reach the  
132 tropopause, while a selected case from the Seoul area involves comparatively shallow (or  
133 less deep) convective clouds. Via comparisons between these two cases, we aim to identify  
134 mechanisms that control varying aerosol-cloud interactions with cloud types.

135 To examine impacts of aerosols, which act as CCN, on clouds and precipitation in the  
136 cases, numerical simulations are performed, as a way of fulfilling above-described aim.  
137 These simulations use a cloud-system resolving model (CSRM) that has reasonably high  
138 resolutions to resolve cloud-scale processes that are related to cloud microphysics and  
139 dynamics. Hence, these simulations are able to find process-level mechanisms in  
140 association with cloud-scale processes.

141

## 142 **2. Case description**

143

144 In the Seoul area, South Korea, there is an observed mesoscale convective system (MCS)  
145 for a period from 03:00 LST (local solar time) to 18:00 LST December 24<sup>th</sup> 2017. During  
146 this period, there is a recorded moderate amount of precipitation and its maximum  
147 precipitation rate reaches ~ 13 mm hr<sup>-1</sup>. Here, precipitation in the Seoul area is measured  
148 by rain gauges in automatic weather stations (AWSs) (King, 2009). The measurement is

149 performed hourly with a spatial resolution that ranges from  $\sim 1$  km to  $\sim 10$  km. The Seoul  
 150 area is marked by an inner rectangle in Figure 1a and dots in the rectangle in Figure 1a  
 151 mark the selected locations of rain gauges. At 21:00 LST December 23<sup>rd</sup> 2017, synoptic-  
 152 scale features develop in favor of the formation and development of the selected MCS and  
 153 associated moderate rainfall. These features involve the southwesterly low-level jets that  
 154 transport warm and moist air to the Korean Peninsula. The southwesterly low-level jet  
 155 plays an important role in the formation and development of rainfall events in the Korean  
 156 Peninsula by fetching warm and moist air (Hwang and Lee 1993; Lee et al. 1998; Seo et  
 157 al. 2013; Oh et al. 2018).

**Deleted:** in Figure 1a and

**Deleted:** 2

**Deleted:** 2

**Deleted:** A low-pressure trough was over northeast China and the  
 Yellow Sea (Figure 1a). Along the flank of the low-pressure system,  
 there was

**Deleted:** to

**Deleted:** . This warm and moist air is originated from the Yellow  
 Sea and transported

**Deleted:** (Figure 1a).

158 There was another observed MCS case in the Beijing area, China for a period from  
 159 14:00 LST on July 27<sup>th</sup> to 00:00 LST July 28<sup>th</sup> 2015. There is a substantial recorded amount  
 160 of precipitation for this period and its maximum precipitation rate reaches  $\sim 45$  mm  $hr^{-1}$ .  
 161 Here, similar to the situation in the Seoul area, precipitation in the Beijing area is measured  
 162 by rain gauges in AWSs hourly with a spatial resolution that ranges from  $\sim 1$  km to  $\sim 10$  km.  
 163 The Beijing area is marked by an inner rectangle in Figure 1b and dots in the rectangle in  
 164 Figure 1b mark the selected locations of rain gauges. At 09:00 LST July 27<sup>th</sup> 2015,  
 165 synoptic-scale features develop in favor of the formation and development of the selected  
 166 MCS. These features involve the southerly low-level jet that, develops heavy rainfall events  
 167 in the Beijing area by transporting warm and moist air to the area. Synoptic features which  
 168 are described here, are based on reanalysis data that are produced by the Met Office Unified  
 169 Model (Brown et al., 2012) every 6 hours with a  $0.11^\circ \times 0.11^\circ$  resolution.

**Deleted:** Figure 1b and

**Deleted:** 2

**Deleted:** 2

**Deleted:** T

**Deleted:** form

**Deleted:** s and

**Deleted:** (Figure 1b). Note that

**Deleted:** s

**Deleted:** in Figures 1a and 1b

### 171 3. CSRM and simulations

172

#### 173 3.1 CSRM

174

175 The Advanced Research Weather Research and Forecasting (ARW) model (version 3.3.1)  
 176 is used as a CSRM. The ARW model is a compressible model with a nonhydrostatic status.  
 177 A 5th-order monotonic advection scheme is used to advect microphysical variables (Wang  
 178 et al., 2009). The Rapid Radiation Transfer Model (RRTMG; Mlawer et al., 1997; Fouquart  
 179 and Bonnel, 1980) is adopted to parameterize shortwave and longwave radiation in

199 simulations. A microphysics scheme that is used in this study calculates the effective sizes  
 200 of hydrometeors that are fed into the RRTMG, and the RRTMG simulates how these  
 201 effective sizes affect radiation.

202 The CSRM adopts a bin scheme as a way of parameterizing microphysics. The  
 203 Hebrew University Cloud Model (HUCM) detailed in Khain et al. (2011) is the bin scheme.  
 204 A set of kinetic equations is solved by the bin scheme to represent a size distribution  
 205 function for each of seven classes of hydrometeors and aerosols acting as CCN. Hence,  
 206 there are seven size distribution functions for hydrometeors. The seven classes of  
 207 hydrometeors are water drops, three types of ice crystals, which are plates, columns and  
 208 dendrites, snow aggregates, graupel and hail. Drops whose radius is smaller (larger) than  
 209 40  $\mu\text{m}$  are categorized to be droplets (raindrops). There are 33 bins for each size  
 210 distribution in a way that the mass of a particle  $m_j$  in the  $j$  bin is to be  $m_j = 2m_{j-1}$ .

**Deleted:** s

**Deleted:** The hydrometeor classes

**Deleted:** (

**Deleted:** ar

**Deleted:** branch types)

211 A cloud-droplet nucleation parameterization based on Köhler theory represents cloud-  
 212 droplet nucleation. Arbitrary aerosol mixing states and aerosol size distributions can be fed  
 213 to this parameterization. To represent heterogeneous ice-crystal nucleation,  
 214 parameterizations by Lohmann and Diehl (2006) and Möhler et al. (2006) are used. In these  
 215 parameterizations, contact, immersion, condensation-freezing, and deposition nucleation  
 216 paths are all considered by taking into account the size distribution of INPs, temperature  
 217 and supersaturation. Homogeneous droplet freezing is  
 218 considered following the theory developed by Koop et al. (2000).

219

### 220 3.2 Control runs

221

222 For a three-dimensional CSRM simulation of the observed case of convective clouds in the  
 223 Seoul (Beijing) area, i.e., the control-s (control-b) run, a domain just over the Seoul  
 224 (Beijing) area, which is shown in Figure 1a (1b), is used. This domain adopts a 300-m  
 225 resolution. The control-s run is for a period from 03:00 LST to 18:00 LST December 24<sup>th</sup>  
 226 2017, while the control-b run is for a period from 14:00 LST on July 27<sup>th</sup> to 00:00 LST  
 227 July 28<sup>th</sup> 2015. The length of the domain is 170 (140) km in the east-west (north-south)  
 228 direction for the control-s run, and 280 (240) km for the control-b run. There are 100  
 229 vertical layers and these layers employ a sigma coordinate that follows the terrain. The top

**Deleted:** Figure 1a (1b) and

**Deleted:** 2

**Deleted:** 2

238 pressure of the model is 50 hPa for both of the control-s and control-b runs. On average,  
 239 the vertical resolution is ~200 m.

240 Reanalysis data, which are produced by the Met Office Unified Model ([Brown et al.,](#)  
 241 [2012](#)), represent the synoptic-scale features, provide initial and boundary conditions of  
 242 variables such as wind, potential temperature, and specific humidity for the simulations.  
 243 The simulations adopt an open lateral boundary condition. The Noah land surface model  
 244 (LSM; Chen and Dudhia, 2001) calculates surface heat fluxes.

245 The current version of the ARW model is not able to consider the spatiotemporal  
 246 variation of aerosol properties. In order to take into account the spatiotemporal variation of  
 247 aerosol properties, which is typical in metropolitan areas, such as composition and number  
 248 concentration, an aerosol preprocessor, which is able to consider the variability of aerosol  
 249 properties, is developed and used in the simulations. This aerosol preprocessor interpolates  
 250 or extrapolates background aerosol properties in observation data such as aerosol mass  
 251 (e.g., PM<sub>2.5</sub> and PM<sub>10</sub>) into grid points and time steps in the model. In this study, the inverse  
 252 distance weighting method is used for the extrapolation and interpolation of observation  
 253 data including aerosol mass into grid points and time steps in the model. PM stands for  
 254 particulate matter. The mass of aerosols with diameter smaller than 2.5 (10.0)  $\mu\text{m}$  per unit  
 255 volume of the air is PM<sub>2.5</sub> (PM<sub>10</sub>).

256 [There are surface observation sites, which measure aerosol properties, in the domains](#)  
 257 [and these sites are classified into two types; the selected locations of these sites are marked](#)  
 258 [by dots in the inner rectangles in Figure 1. The distance between the observation sites](#)  
 259 [ranges from ~1 km to ~10 km and the time interval between observations is ~10 minutes.](#)  
 260 [More than 90% of the sites belong to the first type of the sites. These first-type sites are](#)  
 261 [managed by the government in South Korea or China, and measure PM<sub>2.5</sub> or PM<sub>10</sub> but not](#)  
 262 [other aerosol properties such as aerosol composition and size distributions. Less than 10%](#)  
 263 [of the sites belong to the second type of the sites. These second-type sites are a part of](#)  
 264 [aerosol robotic network \(AERONET; Holben et al., 2001\) and measure aerosol](#)  
 265 [composition and size distributions. The production of aerosol data in these second-type or](#)  
 266 [AERONET sites is viable only in the presence of the sun. The first-type sites observe PM<sub>2.5</sub>](#)  
 267 [or PM<sub>10</sub> using the beta-ray attenuation method \(Eun et al., 2016; Ha et al., 2019\) and hence,](#)  
 268 [produce PM<sub>2.5</sub> or PM<sub>10</sub> data whether the sun is present or not. PM<sub>2.5</sub>/PM<sub>10</sub> data from the](#)

**Deleted:** PM<sub>2.5</sub> or PM<sub>10</sub>, which are measured by surface observation sites in the domains, is used to consider the variability of aerosol properties. The distance between the observation sites ranges from ~1 km to ~10 km and the time interval between observations of aerosol mass is ~10 minutes; the selected locations of these sites are marked by dots in the inner rectangles in Figure 2. Hence, the variability is represented by fine spatiotemporal resolutions of the sites. The ground sites that are equipped with the aerosol robotic network (AERONET; Holben et al., 2001) are in the domains. Distances between these sites are ~10 km. In this study,

279 ~~first-type sites~~ are used to represent the spatiotemporal variability of aerosols over the  
 280 domains and the simulation periods. To represent aerosol composition and size  
 281 distributions, data from the AERONET sites are employed.

282 The AERONET data are averaged over the AERONET sites at 02:00 LST December  
 283 24<sup>th</sup> 2017 (13:00 LST July 27<sup>th</sup> 2015), which is 1 hour before the observed MCS forms, for  
 284 the Seoul (Beijing) case. Based on the average data, it is assumed that aerosol particles are  
 285 internally mixed with 70 (80) % ammonium sulfate and 30 (20) % organic compound for  
 286 the Seoul (Beijing) case. This mixture is assumed to represent aerosol chemical  
 287 composition in the whole domain and during the entire simulation period. Since ammonium  
 288 sulfate and organic compound are representative components of CCN, it is assumed that  
 289 ~~PM<sub>2.5</sub> and PM<sub>10</sub>, which are from the first-type sites, represent the mass of aerosols that act~~  
 290 ~~as CCN~~ for the Seoul and Beijing areas, respectively. Aerosols reflect, scatter and absorb  
 291 shortwave and longwave radiation before they are activated. This type of aerosol-radiation  
 292 interactions is not taken into account in this study. This is mainly based on the fact that in  
 293 the mixture, there is insignificant amount of radiation absorbers; black carbon is a  
 294 representative radiation absorber. The ~~average AERONET data~~ indicate that the size  
 295 distribution of background aerosols acting as CCN follows the ~~bi-~~modal log-normal  
 296 distribution for ~~both of~~ the Seoul ~~and~~ Beijing cases. ~~Based on the average AERONET data,~~  
 297 ~~it is assumed that for the whole domain and simulation period, the size distribution of~~  
 298 ~~background aerosols acting as CCN follows a shape of distribution with specific size~~  
 299 ~~distribution parameters (i.e., modal radius and standard deviation of each of accumulation~~  
 300 ~~and coarse modes, and the partition of aerosol number among those modes) for each of the~~  
 301 ~~cases.~~ Modal radius of the shape of distribution is 0.110 (0.085) and 1.413 (1.523)  $\mu\text{m}$ ,  
 302 while standard deviation of the shape of distribution is 1.54 (1.63) and 1.75 (1.73) for  
 303 accumulation and coarse modes, respectively, in the Seoul (Beijing) case. The partition of  
 304 aerosol number, which is normalized by the total aerosol number of the size distribution,  
 305 is 0.999 and 0.001 for accumulation and coarse modes, respectively, in ~~both of the cases.~~  
 306 By using PM<sub>2.5</sub> or PM<sub>10</sub>, which is not only from the first-type sites but also interpolated  
 307 and extrapolated to grid points immediately above the surface and time steps, and based on  
 308 the assumption of aerosol composition and size distribution above, ~~which is in turn based~~  
 309 ~~on data from the AERONET sites~~, the background number concentrations of aerosols

**Deleted:** ta

**Deleted:** the mass of aerosols that act as CCN is represented by

**Deleted:** observation

**Deleted:** s

**Deleted:** tri

**Deleted:** (

**Deleted:** )

**Deleted:** as exemplified in Figure 3a (3b)

**Deleted:** I

**Deleted:** the

**Deleted:** Aitken,

**Deleted:** as shown in Figure 3a (3b) for the Seoul (Beijing) case

**Deleted:** 0.015 (0.012),

**Deleted:** ,

**Deleted:** 1.28 (1.10),

**Deleted:** ,

**Deleted:** Aitken,

**Deleted:** 0.555 (0.612),

**Deleted:** 444

**Deleted:** (0.387),

**Deleted:** (0.001)

**Deleted:**

**Deleted:** Aitken,

**Deleted:** Seoul (Beijing)

**Deleted:** The distribution parameters of the assumed shape of the size distribution of background aerosols in Figure 3a (3b) are those that are averaged over the AERONET sites at a time point, which is 1 hour before the observed MCS form, for the Seoul (Beijing) case.

**Deleted:** is

339 acting as CCN are obtained for the simulation for each of the cases. There is no variation  
340 with height in background concentrations of aerosols acting as CCN from immediately  
341 above the surface to the top of the planetary boundary layer (PBL). However, it is assumed  
342 that they decrease exponentially with height from the PBL top upward. With this  
343 exponential decrease, when the altitude reaches the tropopause, background concentrations  
344 of aerosols acting as CCN reduce by a factor of ~10 as compared to those at the PBL top.  
345 The size distribution and composition of aerosols acting as CCN do not vary with height.  
346 Once background aerosol properties (i.e., aerosol number concentrations, size distribution  
347 and composition) are put into each grid point and time step, those properties at each grid  
348 point and time step do not change during the course of the simulations.

349 For the control-s and control-b runs, aerosol properties of INPs are not different from  
350 those of CCN except for the fact that the concentration of background aerosols acting as  
351 CCN is 100 times higher than the concentration of background aerosols acting as INPs at  
352 each time step and grid point, following a general difference between CCN and INPs in  
353 terms of their concentrations (Pruppacher and Klett, 1978).

354 Once clouds form and background aerosols start to be in clouds, those aerosols are  
355 not background aerosols anymore and the size distribution and concentrations of those  
356 aerosols begin to evolve through aerosol sinks and sources that include advection and  
357 aerosol activation (Fan et al., 2009). For example, once aerosols are activated, they are  
358 removed from the corresponding bins of the aerosol spectra. In clouds, after aerosol  
359 activation, aerosol mass starts to be inside hydrometeors and via collision-collection, it  
360 transfers to different types and sizes of hydrometeors. In the end, aerosol mass disappears  
361 in the atmosphere when hydrometeors with aerosol mass touches the surface. In non-cloudy  
362 areas, aerosol size and spatial distributions are designed to be identical to the size and  
363 spatial distributions of background aerosols, respectively. In other words, for this study,  
364 we use “the aerosol recovery method”. In this method, at any grid points, immediately after  
365 clouds disappear entirely, aerosol size distributions and number concentrations recover to  
366 background properties that background aerosols at those points have before those points  
367 are included in clouds. In this way, we can keep concentrations of background aerosols  
368 outside clouds in the simulations at observed counterparts. This enables spatiotemporal  
369 distributions of background aerosols in the simulations to mimic those distributions that

370 are observed and particularly associated with observed aerosol advection in reality. In the  
 371 aerosol recovery method, there is no time interval between the cloud disappearance and the  
 372 aerosol recovery. Here, when the sum of mass of all types of hydrometeors (i.e., water  
 373 drops, ice crystals, snow aggregates, graupel and hail) is not zero at a grid point, that grid  
 374 point is considered to be in clouds. When this sum becomes zero, clouds are considered to  
 375 disappear. Many studies using CSRM have employed this aerosol recovery method. They  
 376 have proven that with the recovery method, reasonable simulations of overall cloud and  
 377 precipitation properties are accomplished (e.g., Morrison and Grabowski, 2011; Lebo and  
 378 Morrison, 2014; Lee et al., 2016; Lee et al., 2018).

379

### 380           **3.3 Additional runs**

381

382 We repeat the control-s run by getting rid of aerosol-advection induced increases in  
 383 concentrations of aerosols acting as CCN as a way of investigating how the aerosol  
 384 advection affects the cloud system in the Seoul area. This repeated run is named the low-  
 385 aerosol-s run. An aerosol layer, which is advected from East Asia or from the west of the  
 386 Seoul area to it, increases aerosol concentrations in the Seoul area. There are stations in  
 387 islands in the Yellow Sea that monitor the aerosol advection (Eun et al., 2016; Ha et al.,  
 388 2019). To monitor and identify the aerosol advection, PM<sub>2.5</sub> which is measured by a station  
 389 in Baekryongdo island in Yellow Sea are compared to those which are measured in stations  
 390 in and around the Seoul area. In Figure 1a, a dot outside the inner rectangle marks the  
 391 island. The time evolution of PM<sub>2.5</sub> measured by the station on the island and the average  
 392 PM<sub>2.5</sub> over stations in the Seoul area, between 07:00 LST on December 22<sup>nd</sup> and 21:00 LST  
 393 on December 24<sup>th</sup> in 2017 when there is the strong advection of aerosols from East Asia to  
 394 the Seoul area, is shown in Figure 2. At 09:00 LST on December 22<sup>nd</sup>, the advection of  
 395 aerosols from East Asia enables aerosol mass to start going up and attain its peak around  
 396 05:00 LST on December 23<sup>rd</sup> on the island. Following this, aerosol mass starts to increase  
 397 in the Seoul area around 01:00 LST on December 23<sup>rd</sup>, and the mass attains its peak at  
 398 15:00 LST on December 23<sup>rd</sup> in the Seoul area. This is because aerosols, which are  
 399 advected from East Asia, move through the island to reach the Seoul area.

**Deleted: 2**

**Deleted: 4**

402 In the low-aerosol-s run, as a way of getting rid of aerosol-advection induced increases  
 403 in concentrations of aerosols acting as CCN, it is assumed that PM<sub>2.5</sub>, which is assumed to  
 404 represent the mass of aerosols acting as CCN, and the associated background concentration  
 405 of aerosols acting as CCN after 01:00 LST on December 23<sup>rd</sup> do not evolve with the aerosol  
 406 advection in the Seoul area. Hence, the background concentration of aerosols acting as  
 407 CCN is assumed to have that at 01:00 LST on December 23<sup>rd</sup> at each time step and grid  
 408 point at the beginning of the simulation period. However, to isolate CCN effects on clouds,  
 409 background aerosol concentration acting as INPs at each time step and grid point in the  
 410 low-aerosol-s run is not different from that in the control-s run during the simulation period.  
 411 In the observed PM data for the Seoul area, there is reduction in PM by a factor of ~10 on  
 412 average over a period between ~07:00 and ~14:00 LST on December 24<sup>th</sup>, since  
 413 precipitation scavenges aerosols (Figure 2). To emulate this scavenging and reflect it in  
 414 background aerosols acting as CCN for the low-aerosol-s run, PM<sub>2.5</sub> and corresponding  
 415 background concentrations of aerosols acting as CCN at each grid point is gradually  
 416 reduced for the period between 07:00 and 14:00 LST on December 24<sup>th</sup>. This reduction is  
 417 done in a way that background concentrations of aerosols acting as CCN at each grid point  
 418 at 14:00 LST on December 24<sup>th</sup> is 10 times lower than that at 07:00 LST on December 24<sup>th</sup>  
 419 in the low-aerosol-s run. Then, PM<sub>2.5</sub> and corresponding background concentrations of  
 420 aerosols acting as CCN at each grid point at 14:00 LST on December 24<sup>th</sup> maintains until  
 421 the end of the simulation period. This results in the evolution of the average PM<sub>2.5</sub> over the  
 422 Seoul area in the low-aerosol-s run as shown in Figure 2. Here, the concentration of  
 423 background aerosols acting as CCN, which is averaged over the whole domain and  
 424 simulation period, in the control-s run is 3.1 times higher than that in the low-aerosol-s run.  
 425 Via comparisons between the runs, how the increasing concentration of background  
 426 aerosols acting as CCN due to the aerosol advection has an impact on clouds can be  
 427 examined. The concentration of background aerosols acting as CCN is different among  
 428 grid points and time steps in the control-s run. Hence, the ratio of the concentration of  
 429 background aerosols acting as CCN between the runs is different among grid points and  
 430 time steps.

431 For the Beijing case, to examine how aerosols acting as CCN affect clouds and  
 432 precipitation, we repeat the control-b run with simply reduced concentrations of

Deleted: 4

Deleted: 4

435 background aerosols acting as CCN at each time step and grid point by a factor of 3.1. This  
 436 repeated run is named the low-aerosol-b run. The 3.1-fold increase in aerosol  
 437 concentrations from the low-aerosol-b run to the control-b is based on the 3.1-fold increase  
 438 in the average concentration of background aerosols acting as CCN from the low-aerosol-  
 439 s run to the control-s run. However, as in the control-s and low-aerosol-s runs, to isolate  
 440 CCN effects on clouds, background aerosol concentration acting as INPs at each time step  
 441 and grid point in the low-aerosol-b run is identical to that in the control-b run during the  
 442 simulation period. Hence, on average, a pair of the control-s and low-aerosol-s runs has the  
 443 same perturbation of aerosols acting as CCN as in a pair of the control-b and low-aerosol-  
 444 b runs. Here, we define aerosol perturbation as a relative increase in aerosol concentration  
 445 when compared to that before the increase occurs. The brief summary of all simulations in  
 446 this study is given in Table 1.

447

#### 448 4. Results

449

##### 450 4.1 Cumulative precipitation

451

452 We compare the observed precipitation to the simulated counterpart in the control-s run for  
 453 the Seoul case and in the control-b run for the Beijing case. For this comparison, the  
 454 observed and simulated precipitation rates at the surface are averaged over the domain for  
 455 each of the Seoul and Beijing cases (Figures 3a and 3b). Here, the simulated precipitation  
 456 rates are smoothed over 1 hour. The comparison shows that the evolution of the simulated  
 457 precipitation rate does not deviate from the observed counterpart significantly (Figures 3a  
 458 and 3b).

Deleted: 5

Deleted: 5

Deleted: 5

Deleted: 5

459 In the Seoul case, overall, the precipitation rate is higher in the control-s run than in  
 460 the low-aerosol-s run. As a result of this, the domain-averaged cumulative precipitation  
 461 amount at the last time step is 14.1 mm and 12.0 mm in the control-s run and the low-  
 462 aerosol-s run, respectively. The control-s run shows ~20 % higher cumulative precipitation  
 463 amount. In the Beijing case, the evolution of the mean precipitation rate in the control-b  
 464 run is not significantly different from that in the low-aerosol-b run. Due to this, the control-  
 465 b run shows only ~2 % higher cumulative precipitation amount, despite the fact that the

470 concentrations of background aerosols acting as CCN are  $\sim 3$  times higher in the control-b  
 471 run than in the low-aerosol-b run. Note that in the Seoul case, the time- and domain-  
 472 averaged concentration of background aerosols acting as CCN is also  $\sim 3$  times higher in  
 473 the control-s run than in the low-aerosol-s run. Despite this, the difference in the cumulative  
 474 precipitation amount between the runs with different concentrations of background  
 475 aerosols acting as CCN is greater in the Seoul case than in the Beijing case.

476

#### 477 **4.2 Precipitation, and associated latent-heat and dynamic processes**

478

479 Figures 4a and 4b show the cumulative frequency distributions of precipitation rates at the  
 480 last time step in the simulations for the Seoul and Beijing cases, respectively. In each of  
 481 those figures, the observed frequency distribution is shown and compared to the simulated  
 482 distribution. The observed distribution is obtained by interpolating and extrapolating the  
 483 observed precipitation rates to grid points and time steps in each of the control-s and  
 484 control-b runs. The observed maximum precipitation rates are 13.0 and 44.5  $\text{mm hr}^{-1}$  for  
 485 the Seoul and Beijing cases, respectively, and these maximum rates are similar to those in  
 486 the control-s and control-b runs, respectively. Overall, the observed and simulated  
 487 frequency distributions are in good agreement for each of the cases. This enables us to  
 488 assume that results in the control-s (control-b) run are benchmark results to which results  
 489 in the low-aerosol-s (low-aerosol-b) run can be compared to identify how aerosols acting  
 490 as CCN have an impact on clouds and precipitation for the Seoul (Beijing) case. Here, it is  
 491 notable that for the Beijing case, while differences in the cumulative precipitation amount  
 492 between the control-b and low-aerosol-b runs are not significant, features in the frequency  
 493 distribution of precipitation rates between those runs are substantially different (Figure 4b).

494

##### 495 **1) Seoul case**

496

###### 497 **a. Precipitation Frequency distributions**

498

499 Regarding precipitation whose rates are higher than  $\sim 2 \text{ mm hr}^{-1}$ , the cumulative  
 500 precipitation frequency at the last time step is higher in the control-s run as compared to

**Deleted: 6**

**Deleted: 6**

**Deleted: 6**

504 that in the low-aerosol-s run (Figure 4a). In particular, for the precipitation rate of  $11.4 \text{ mm}$   
 505  $\text{h}^{-1}$ , there is an increase in the cumulative frequency by a factor of as much as  $\sim 10$  in the  
 506 control-s run. When it comes to precipitation rates above  $11.5 \text{ mm hr}^{-1}$ , precipitation is  
 507 present in the control-s run and precipitation is absent in the low-aerosol-s run. Regarding  
 508 precipitation whose rates are lower than  $\sim 2 \text{ mm hr}^{-1}$ , differences in the cumulative  
 509 frequency between the runs are insignificant. Hence, we see that there are significant  
 510 increases in the frequency of relatively heavy precipitation whose rates are above  $\sim 2 \text{ mm}$   
 511  $\text{hr}^{-1}$  in the control-s run when compared to that in the low-aerosol-s run. At the last time  
 512 step, this results in a larger amount of cumulative precipitation in the control-s run than in  
 513 the low-aerosol-s run.

514 The time evolution of the cumulative precipitation frequency is shown in Figure 5. At  
 515 06:00 LST December 24<sup>th</sup> 2017, which corresponds to the initial stage of the precipitation  
 516 development, the maximum precipitation rate reaches  $\sim 3 \text{ mm hr}^{-1}$  and there is the greater  
 517 frequency over most of precipitation rates in the control-s run than in the low-aerosol-s run  
 518 (Figure 5a). With the time progress from 06:00 LST to 10:00 LST, the maximum  
 519 precipitation rate increases to reach  $12 \text{ mm hr}^{-1}$  and the cumulative frequency is higher over  
 520 precipitation whose rates are higher than  $\sim 3 \text{ mm hr}^{-1}$  in the control-s run, while for  
 521 precipitation whose rates are lower than  $\sim 3 \text{ mm hr}^{-1}$ , differences in the cumulative  
 522 frequency between the runs are negligible (Figures 5a and 5b). When time reaches 12:00  
 523 LST, which is around time when the peak in the evolution of the area-averaged  
 524 precipitation rates occurs and thus the system is at its mature stage, the maximum  
 525 precipitation rate increases up to  $\sim 13 \text{ mm hr}^{-1}$  (Figures 3a and 5c). The basic patterns of  
 526 differences in the cumulative precipitation frequency between the runs with the maximum  
 527 precipitation rate around  $13 \text{ mm hr}^{-1}$ , which are established at 12:00 LST, maintain until  
 528 the end of the simulation period (Figures 4a and 5c).

529

### 530       b. Condensation, deposition, updrafts and associated variables

531

532 Note that the source of precipitation is precipitable hydrometeors which are raindrops,  
 533 snow, graupel and hail particles. Droplets and ice crystals are the source of those  
 534 precipitable hydrometeors mostly via collision and coalescence processes. Droplets and ice

Deleted: 6

Deleted: 7

Deleted: 7

Deleted: 7

Deleted: 7

Deleted: 5

Deleted: 7

Deleted: 6

Deleted: 7

544 crystals gain their mass mostly via condensation and deposition. Based on this, to explain  
 545 the greater cumulative precipitation amount in the control-s run than in the low-aerosol-s  
 546 run, the evolutions of differences in condensation, deposition and associated updrafts  
 547 between the runs are analyzed. The vertical profiles of differences in the area-averaged  
 548 condensation, deposition and freezing rates, updraft mass fluxes and the associated mass  
 549 density of each class of hydrometeors between the runs at 03:20, 03:40, 06:00 and 12:00  
 550 LST are shown in Figure 6. In Figure 6, differences in freezing rates are added for a more  
 551 comprehensive understanding of processes that are related to differences in cumulative  
 552 precipitation amount between the runs. Freezing includes riming processes between liquid  
 553 and solid hydrometeors and these riming processes act as a source of precipitable  
 554 hydrometeors. Cloud fractions are 0.32 (0.30), 0.85 (0.82), 0.93 (0.92) and 1.00 (1.00) in  
 555 the control-s (low-aerosol-s) run at 03:20, 03:40, 06:00 and 12:00 LST, respectively. We  
 556 see that cloud fraction varies 0~6% between the runs. Note that in all of figures, which  
 557 display snow and hail mass density and include Figure 6, snow mass density includes ice-  
 558 crystal mass density, while hail mass density includes graupel mass density for the sake of  
 559 the display brevity. In Figure 6, horizontal black lines represent the altitudes of freezing  
 560 and melting.

**Deleted:** 8  
**Deleted:** 8

**Deleted:** does not vary significantly between the runs.

**Deleted:** 8

**Deleted:** 8

**Deleted:** 8

**Deleted:** 8

**Deleted:** 8

561 Condensation rates in the control-s run start to be larger than that in the low-aerosol-  
 562 s run at 03:20 LST (Figure 6a). Higher aerosol or CCN concentrations induce more  
 563 nucleation of droplets, higher cloud droplet number concentration (CDNC) and associated  
 564 greater integrated surface of droplets in the control-s run. CDNC, which is averaged over  
 565 grid points and time steps with non-zero CDNC, is 1050 and 352 cm<sup>-3</sup> in the control-s and  
 566 low-aerosol-s runs, respectively. Hence, more droplet surface is provided for water vapor  
 567 to condense onto in the control-s run. This leads to more condensation in the control-s run.  
 568 This establishes stronger feedbacks between updrafts and condensation, leading to greater  
 569 droplet (or cloud-liquid) mass at 03:20 LST in the control-s run (Figure 6a). Then, these  
 570 stronger feedbacks, which involve stronger updrafts particularly above 2 km in altitude,  
 571 subsequently induce greater deposition and snow mass as time progresses from 03:20 LST  
 572 to 03:40 LST, while more condensation and greater droplet mass maintain in the control-s  
 573 run with the time progress to 03:40 LST (Figure 6b). These stronger updrafts enable clouds  
 574 to grow higher in the control-s run. This eventually leads to a situation where the maximum

583 cloud depth is  $\sim$ 7 km in the control-s run and this depth is  $\sim$ 5 % deeper than that in the low-  
 584 aerosol-s run for the whole simulation period.

585 Through aerosol-induced stronger feedbacks between condensation, deposition and  
 586 updrafts in the control-s run, while more condensation and more overall deposition  
 587 maintain in the control-s run, differences in condensation and deposition between the  
 588 control-s and low-aerosol-s runs increase as time progresses from 03:40 LST to 06:00 LST  
 589 (Figures 6b and 6c). Associated with this, the greater mass of raindrops and hail particles  
 590 appears up, while the greater mass of droplets and snow in the control-s run than in the  
 591 low-aerosol-s run maintains with the time progress from 03:40 LST to 06:00 LST (Figure  
 592 6c). At 06:00 LST, there is more freezing starting to occur in the control-s run than in the  
 593 low-aerosol-s run. However, differences in freezing are  $\sim$ one and  $\sim$ two orders of magnitude  
 594 smaller than those in deposition and condensation, respectively. After 06:00 LST until time  
 595 reaches 12:00 LST when the overall differences in the cumulative precipitation frequency  
 596 between the runs are established, differences in freezing become  $\sim$ 3 times smaller than  
 597 those in deposition and  $\sim$ one order of magnitude smaller than those in condensation,  
 598 (Figures 6c and 6d). The greater mass of hydrometeors in the control-s run also continues  
 599 after 06:00 LST until time reaches 12:00 LST (Figures 6c and 6d). At 12:00 LST,  
 600 condensation, deposition and freezing rates are still higher in the control-s run. Here, we  
 601 see that CCN-induced more cumulative precipitation amount and associated differences in  
 602 the precipitation frequency distribution between the control-s and low-aerosol-s runs are  
 603 primarily associated with CCN-induced more condensation, which induce CCN-induced  
 604 more deposition and higher mass density of hydrometeors as sources of precipitation, but  
 605 weakly connected to CCN-induced changes in freezing. This is supported by the fact that  
 606 the time- and domain-averaged differences in freezing rate are  $\sim$ one to  $\sim$ two order of  
 607 magnitude smaller than those in condensation and deposition rates.

608

609 **c. Condensation frequency distributions and horizontal distributions of**  
 610 **condensation and precipitation**

611

612 Based on the importance of condensation for CCN-induced changes in precipitation, the  
 613 horizontal distribution of the column-averaged condensation rates over the domain and the

**Deleted:** 8

**Deleted:** 8

**Deleted:** 8

**Deleted:**

**Deleted:** at an order of magnitude, which is similar to that of  
 differences in deposition, and become around one order of  
 magnitude smaller than those in condensation

**Deleted:** 8

**Deleted:** 8

**Deleted:**

**Deleted:** 8

**Deleted:** 8

626 cumulative frequency distribution of the column-averaged condensation rates at each time  
 627 step is obtained. To better visualize the role of condensation in precipitation, the horizontal  
 628 distribution of the column-averaged condensation rates is superimposed on that of  
 629 precipitation rates (Figure 7). At 03:40 LST, condensation mainly occurs around the  
 630 northern part of the domain as marked by a yellow rectangle. The synoptic wind condition  
 631 in the marked area favors the collision between northward and southward wind and the  
 632 associated convergence around the surface (Figures 7a and 7b). This convergence induces  
 633 updrafts and condensation in the marked area. In the marked area, more aerosols acting as  
 634 CCN induce more and more extensive condensation, which leads to the higher domain-  
 635 averaged condensation rates in the control-s run than in the low-aerosol-s run (Figures 6b,  
 636 7a and 7b). More droplets are formed on more aerosols acting as CCN and more droplets  
 637 provide more surface areas where condensation occurs and this enables more and more  
 638 extensive condensation in the control-s run than in the low-aerosol-s run (Figures 6b, 7a  
 639 and 7b).

640 At 06:20 LST, a precipitating system is advected into the domain via the western  
 641 boundary, and as seen in Figures 7c and 7d for 08:40 LST, as time progresses to 08:40 LST,  
 642 the advected precipitating system is further advected to the east and extended mostly over  
 643 areas in the northern part of the domain where condensation mainly occurs. This confirms  
 644 that condensation is the main source of cloud mass and precipitation. In the eastern part of  
 645 the domain, there are mountains and in particular, higher mountains are on the northeastern  
 646 part of the domain than in the other parts of the domain. These higher mountains induce  
 647 forced convection and associated condensation more effectively in the northeastern part  
 648 than in the other parts. This is in favor of the precipitating system that extends further to  
 649 the east in the northern part of the domain. Due to more aerosols acting as CCN,  
 650 condensation, which is induced by forced convection over mountains, is more and more  
 651 extensive in the control-s run (Figures 7c and 7d). In association with this, there is more  
 652 extension of the precipitating system in the control-s run than in the low-aerosol-s run. This  
 653 enables the system in the control-s run to reach the eastern boundary at 08:40 LST, which  
 654 is earlier than in the low-aerosol-s run (Figures 7c and 7d). The system in the low-aerosol-  
 655 s run reaches the eastern boundary at 09:00 LST. Here, we see that although aerosols acting  
 656 as CCN do not change overall locations of the precipitation system, they affect how fast

**Deleted: 9**

**Deleted: 9**

**Deleted: 9**

**Deleted: 8**

**Deleted: 9**

**Deleted: 9**

**Deleted: 8**

**Deleted: 9**

**Deleted: 9**

**Deleted: 9**

**Deleted: c**

**Deleted: 9**

**Deleted: d**

**Deleted: 7**

**Deleted: 2**

**Deleted: 7**

**Deleted: 2**

**Deleted: 9**

**Deleted: c**

**Deleted: 9**

**Deleted: d**

**Deleted: 1**

As time progresses to 08:40 LST, the precipitating system moves eastward further in the northern part of the domain and the system in the control-s run extends to the east further as compared to that in the low-aerosol-s run (Figures 9e and 9f).

**Deleted:**

**Deleted:** more aerosols acting as CCN and associated more condensation over mountains in the northeastern part

**Deleted: 9**

**Deleted: e**

**Deleted: 9**

**Deleted: f**

690 the system extends to the east by affecting the amount of condensation which is produced  
 691 by forced convection. Associated with this, as seen in Figure 8, the control-s run has the  
 692 much higher cumulative condensation frequency than the low-aerosol-s run over all of  
 693 condensation rates during the period between 07:20 and 09:00 LST. Contributed by this,  
 694 the higher precipitation frequency over most of precipitation rates occurs in the control-s  
 695 run during and after the period (Supplementary Figures 1a and 1b and Figures 5b and 5c).

**Deleted: 10**

696 At 10:00 LST, in the southern part of the domain, there is a precipitating area forming  
 697 as marked by a yellow rectangle (Figures 7e and 7f). The precipitation area in the southern  
 698 part of the domain extends and merges into the advecting main precipitating system in the  
 699 northern part of the domain. The merge leads to precipitation that occupies most of the  
 700 domain at 12:00 LST (Figures 7g and 7h). After 10:00 LST, associated with this merge,  
 701 the maximum precipitation rate increases to  $13 \text{ mm hr}^{-1}$  at 12:00 LST (Figures 5c). After  
 702 13:00 LST, the precipitation enters its dissipating stage and its area reduces and nearly  
 703 disappears. Even after the merge, CCN-induced more condensation maintains and this in  
 704 turn contributes to a situation where the control-s run has the greater precipitation  
 705 frequency over most of precipitation rates than in the low-aerosol-s run until the  
 706 simulations progress to their last time step (Figures 4a, 5c and 6d).

**Deleted: 7**

**Deleted: 7**

**Deleted: 9**

**Deleted: g**

**Deleted: 9**

**Deleted: h**

**Deleted: as time progresses to 11:00 LST (Figures 9i and 9j).**

**Deleted: 9**

**Deleted: k**

**Deleted: 9**

**Deleted: l**

**Deleted: 7**

**Deleted: 6**

**Deleted: 7**

**Deleted: 8**

## 708 2) Beijing case

709  
 710 Stronger convection and deeper clouds develop in the Beijing case than in the Seoul case.  
 711 The maximum cloud depth is  $\sim 7$  and  $\sim 12$  km in the control-s and control-b runs,  
 712 respectively. In the Seoul case, clouds do not reach the tropopause, while they reach the  
 713 tropopause in the Beijing case. Deeper clouds in the Beijing case produce the maximum  
 714 precipitation rate of  $\sim 45 \text{ mm hr}^{-1}$  in the control-b run. However, less deep clouds in the  
 715 Seoul case produce the maximum precipitation rate of  $\sim 13 \text{ mm hr}^{-1}$  in the control-s run  
 716 (Figure 4).

**Deleted: 6**

### 718 a. Precipitation frequency distributions

719

737 When it comes to precipitation whose rates are higher than  $\sim 12 \text{ mm hr}^{-1}$ , the control-b run  
 738 has the higher cumulative precipitation frequency at the last time step than the low-aerosol-  
 739 b run (Figure 4b). Particularly, for the precipitation rates of 28.1 and 30.0  $\text{mm hr}^{-1}$ , the  
 740 cumulative frequency increases by a factor of as much as  $\sim 10$ . Moreover, regarding  
 741 precipitation rates higher than  $\sim 33 \text{ mm hr}^{-1}$ , precipitation is present in the control-b run,  
 742 however, precipitation is absent in the low-aerosol-b run. Hence, we see that the frequency  
 743 of comparatively heavy precipitation whose rates are higher than  $\sim 12 \text{ mm hr}^{-1}$  rises  
 744 significantly in the control-b run as compared to that in the low-aerosol-b run. Below  $\sim 2$   
 745  $\text{mm hr}^{-1}$ , there is also the greater precipitation frequency in the control-b run than in the  
 746 low-aerosol-b run. Unlike the situation for precipitation rates above  $\sim 12 \text{ mm hr}^{-1}$  and below  
 747  $\sim 2 \text{ mm hr}^{-1}$ , for precipitation rates from  $\sim 2 \text{ mm hr}^{-1}$  to  $\sim 12 \text{ mm hr}^{-1}$ , the control-aerosol-b  
 748 run has the lower precipitation frequency than in the low-aerosol-b run. Here, we see that  
 749 the higher precipitation frequency above  $\sim 12 \text{ mm hr}^{-1}$  and below  $\sim 2 \text{ mm hr}^{-1}$  balances out  
 750 the lower precipitation frequency between  $\sim 2$  and  $\sim 12 \text{ mm hr}^{-1}$  in the control-b run. This  
 751 results in the similar cumulative precipitation amount between the runs.

**Deleted: 6**

752 Figure 9 shows the time evolution of the cumulative precipitation frequency. When  
 753 precipitation starts around 16:00 LST, the higher precipitation frequency occurs over most  
 754 of precipitation rates in the low-aerosol-run-b run than in the control-b run (Figure 9a). At  
 755 16:00 LST, the maximum precipitation rate is lower than  $1.0 \text{ mm hr}^{-1}$  for both of the runs.  
 756 As time progresses to 17:00 LST, the maximum precipitation rate increases to  $\sim 17 \text{ mm hr}^{-1}$   
 757 and the higher (lower) cumulative precipitation frequency over precipitation rates higher  
 758 than  $\sim 12 \text{ mm hr}^{-1}$  (between  $\sim 2$  and  $\sim 12 \text{ mm hr}^{-1}$ ) in the control-b run than in the low-  
 759 aerosol-b run, which is described above as shown in Figure 4b for the last time step, starts  
 760 to emerge (Figure 9b). At 17:20 LST, the higher frequency for precipitation rates below  $2$   
 761  $\text{mm hr}^{-1}$  in the control-b run, which is also described above as shown in Figure 4b for the  
 762 last time step, starts to show up, while the higher (lower) frequency for precipitation rates  
 763 higher than  $\sim 12 \text{ mm hr}^{-1}$  (between  $\sim 2$  and  $\sim 12 \text{ mm hr}^{-1}$ ) in the control-b run, which is  
 764 established at 17:00 LST, maintains as time progresses from 17:00 LST to 17:20 LST  
 765 (Figure 9c). At 17:20 LST, the maximum precipitation rate increases to  $42$  ( $19$ )  $\text{mm hr}^{-1}$  in  
 766 the control-b (low-aerosol-b) run (Figure 9c). At 19:00 LST, the maximum precipitation  
 767 rate increases to  $\sim 45$  ( $33$ )  $\text{mm hr}^{-1}$  for the control-b (low-aerosol-b) run, while the

**Deleted: 11**

**Deleted: 11**

**Deleted: 6**

**Deleted: 11**

**Deleted: 6**

**Deleted: 11**

**Deleted: 11**

776 qualitative nature of differences in the precipitation frequency distributions with the tipping  
 777 precipitation rates of  $\sim 2$  and  $\sim 12$  mm  $hr^{-1}$  between the runs does not vary much between  
 778 17:20 and 19:00 LST (Figures 9c and 9d). The qualitative nature of differences in the  
 779 cumulative precipitation frequency between the runs and the maximum precipitation rates  
 780 in each of the runs, which are established at 19:00 LST, do not vary significantly until the  
 781 end of the simulation period (Figures 4b and 9d).  
 782

**Deleted: 11**

**Deleted: 11**

**Deleted: 6**

**Deleted: 11**

### 783       b. Condensation, deposition, updrafts and associated variables

784  
 785 As done for the Seoul case, as a way of better understanding differences in the cumulative  
 786 precipitation amount and frequency between the control-b and low-aerosol-b runs, the  
 787 evolutions of differences in the vertical distributions of the area-averaged condensation  
 788 rates, deposition rates, freezing rates, the mass density of each class of hydrometeors and  
 789 updrafts mass fluxes are obtained and shown in Figures 10. Cloud fractions are 0.12 (0.11),  
 790 0.25 (0.22), 0.36 (0.32), 0.43 (0.40) and 0.48 (0.47) in the control-b (low-aerosol-b) run at  
 791 14:20, 15:40, 16:00, 17:20 and 19:00 LST, respectively. Here, we see that cloud fraction  
 792 varies by  $\sim 2\text{-}12\%$  between the runs. In Figure 10, horizontal black lines represent the  
 793 altitudes of freezing and melting. As seen in Figure 3b, precipitation starts around 16:00  
 794 LST but differences in condensation rates start at 14:20 LST with higher condensation rates  
 795 in the control-b run (Figure 10a). Similar to the situation in the Seoul case, higher  
 796 concentrations of aerosols acting as CCN induce more nucleation of droplets, higher  
 797 CDNC and associated greater integrated surface of droplets in the control-b run. CDNC,  
 798 which is averaged over grid points and time steps with non-zero CDNC, is 992 and 341  
 799  $cm^{-3}$  in the control-b and low-aerosol-b runs, respectively. Hence, more droplet surface is  
 800 provided for water vapor to condense onto in the control-b run. This leads to more  
 801 condensation in the control-b run. Due to this, cloud-liquid or droplet mass becomes greater  
 802 in the control-b run at 14:20 LST (Figure 10a). Increased condensation rates induce  
 803 increased condensational heating and thus intensified updrafts (Figure 10a). These  
 804 updrafts enable the maximum cloud depth to be  $\sim 12$  km in the control-b run and this depth  
 805 is just  $\sim 1\%$  deeper than that in the low-aerosol-b run for the whole simulation period. This  
 806 negligible difference in the maximum cloud depth between the runs is due to the fact that

**Deleted: 2**

**Deleted:**

**Deleted:** cloud fraction does not vary significantly between the runs...

**Deleted: 2**

**Deleted: 5**

**Deleted: 2**

**Deleted: 2**

**Deleted: 2**

820 clouds with the maximum depth reach the tropopause in both of runs and thus there is not  
 821 much wiggle room to make significant differences in cloud depth between the runs.

822 When time reaches 15:40 LST, deposition rates and snow mass start to show  
 823 differences between the runs, while higher condensation rates and droplet mass maintain  
 824 in the control-b run with the time progress from 14:20 LST to 15:40 LST. However, unlike  
 825 the situation in the Seoul case, higher concentrations of aerosols acting as CCN result in  
 826 lower deposition rates and snow mass in the control-b run (Figure 10b). When time  
 827 progresses from 15:40 LST to 16:00 LST, differences in freezing start to occur and freezing  
 828 rates are lower (higher) at altitudes between  $\sim$ 6 and  $\sim$ 8 km ( $\sim$ 4 and  $\sim$ 6 km), while higher  
 829 condensation rates and droplet mass, and lower snow mass maintain in the control-b run  
 830 (Figure 10c). Due to stronger updrafts, which are mainly ascribed to more condensation,  
 831 deposition rates start to be higher at altitudes between  $\sim$ 7 and  $\sim$ 9 km and freezing rates are  
 832 higher at altitudes between  $\sim$ 4 and  $\sim$ 6 km in the control-b run with the time progress from  
 833 15:40 LST to 16:00 LST (Figure 10c). Differences in freezing rates are similar to those in  
 834 deposition and  $\sim$ two orders of magnitude smaller than those in condensation at 16:00 LST  
 835 (Figure 10c). At 16:00 LST, differences in hail mass between the runs appear up and hail  
 836 mass is slightly lower in the control-b run (Figure 10c). At 17:20 LST, overall, freezing  
 837 rates are lower at altitudes between  $\sim$ 4 and  $\sim$ 8 km, while overall, snow and hail mass is still  
 838 lower, and droplet mass is still higher in the control-b run (Figure 10d). Differences in  
 839 freezing rates are  $\sim$ 2 times smaller than those in deposition and  $\sim$ one order of magnitude  
 840 smaller than those in condensation at 17:20 LST (Figure 10d). Due to more condensation  
 841 and droplet mass, greater raindrop mass appears up in the control-b run at 17:20 LST  
 842 (Figure 10d). As the time progresses to 19:00 LST, deposition rates become lower at the  
 843 altitudes from  $\sim$ 7 km to  $\sim$ 12 km and overall freezing rates become higher at altitudes from  
 844  $\sim$  4 km to  $\sim$ 10 km in the control-b run (Figure 10e). Overall, lower snow and hail mass  
 845 maintains in the control-b run as time progresses from 17:20 LST to 19:00 LST. As time  
 846 progresses from 17:20 LST to 19:00 LST, overall higher condensation rates, droplet and  
 847 raindrop mass maintain in the control-b run (Figure 10e). Here, while the time- and  
 848 domain-averaged deposition (condensation and freezing) rates are lower (higher) in the  
 849 control-b run over the whole simulation period, the average differences in freezing rates  
 850 are  $\sim$ one to  $\sim$ two orders of magnitude smaller than those in deposition and condensation

**Deleted:** 2

**Deleted:** 2

**Deleted:** at the same order of magnitude of

**Deleted:** 2

**Deleted:** 2

**Deleted:**

**Deleted:** 2

**Deleted:** at the same order of magnitude of

**Deleted:** s

**Deleted:** 2

**Deleted:** 2

**Deleted:**

**Deleted:** 2

**Deleted:** 2

867 rates between the runs. Hence, more condensation (but not deposition and freezing) is a  
 868 main cause of stronger updrafts in the control-b run. More condensation and more freezing  
 869 tend to induce increases in the mass of precipitable hydrometeors in the control-b run. Less  
 870 deposition tends to induce decreases in the mass of precipitable hydrometeors in the  
 871 control-b run. This competition between condensation, deposition and freezing leads to  
 872 negligible differences in the cumulative precipitation amount at the last time step between  
 873 the control-b and low-aerosol-b runs, although roles of freezing in this competition are  
 874 negligible as compared to those of condensation and deposition.

875

876 **c. Condensation frequency distributions, horizontal distributions of  
 877 condensation and precipitation, and condensation-precipitation  
 878 correlations**

879

880 Figure 11 shows the horizontal distribution of the column-averaged condensation rates over  
 881 the domain and Figure 12 shows the cumulative frequency distributions of column-  
 882 averaged condensation rates at selected times. As in the Seoul case, the horizontal  
 883 distribution of condensation rates is superimposed on that of precipitation rates and the  
 884 terrain in Figure 11. At 14:20 LST, condensation starts to occur in places with mountains,  
 885 which induce forced convection, and condensation is concentrated around the center of the  
 886 domain as marked by a yellow circle (Figures 11a and 11b). Note that condensation does  
 887 not occur in the plain area which is the south of the 100-m terrain-height contour line  
 888 (Figures 11a and 11b). Due to higher concentrations of aerosols acting as CCN, there is  
 889 more condensation around the center in the control-b run than in the low-aerosol-b run  
 890 (Figures 11a and 11b). This leads to a situation where the control-b run has the higher area-  
 891 averaged condensation rates than the low-aerosol-b run (Figure 10a). Then, as time  
 892 progresses to 17:20 LST, the condensation area extends to the eastern and western parts of  
 893 the domain mostly over mountain areas (Figures 11c and 11d). Hence, the main source of  
 894 condensation is considered to be forced convection over mountains. As seen in Figures 11c  
 895 and 11d, higher concentrations of aerosols acting as CCN induce the control-b run to have  
 896 much more condensation spots and thus much bigger areas with condensation than the low-  
 897 aerosol-b run at 17:20 LST. Associated with this, CCN-induced more condensation in the

**Deleted: 3**

**Deleted: 4**

**Deleted: 3**

**Deleted: 3**

**Deleted: 3**

**Deleted: 3**

**Deleted: 3**

**Deleted: 3**

**Deleted: 2**

**Deleted: 3**

**Deleted: 3**

**Deleted: 3**

**Deleted: 3**

912 control-b run maintains with the time progress to 17:20 LST (Figure 10d). At 17:20 LST,  
 913 precipitation mainly occurs in a spot which is in the western part of areas with relatively  
 914 high condensation rates (Figures 11c and 11d).

**Deleted: 2**

915 At 17:20 LST, as seen in the cumulative frequency of condensation rates, the control-  
 916 b run has the higher condensation frequency above condensation rate of  $\sim 10 \times 10^{-3} \text{ g m}^{-3} \text{ s}^{-1}$   
 917 and below that of  $\sim 3 \times 10^{-3} \text{ g m}^{-3} \text{ s}^{-1}$  than the low-aerosol-b run (Figure 12a). This pattern  
 918 of differences in the condensation frequency distribution with the tipping condensation-  
 919 rate points at  $\sim 10 \times 10^{-3}$  and  $\sim 3 \times 10^{-3} \text{ g m}^{-2} \text{ s}^{-1}$  continues up to 19:00 LST (Figures 12b).

**Deleted: 3**

**Deleted: 3**

**Deleted: 4**

920 Figure 13 shows the mean precipitation rate over each of the column-averaged  
 921 condensation rates for the period up to 17:20 LST in the control-b run. A column-averaged  
 922 condensation rate in an air column with a precipitation rate at its surface is obtained and  
 923 these condensation and precipitation rates are paired at each column and time step. Then,  
 924 collected precipitation rates are classified and grouped based on the corresponding paired  
 925 column-averaged condensation rates. The classified precipitation rates corresponding to  
 926 each of the column-averaged condensation rates are averaged arithmetically to construct  
 927 Figure 13. There are only less than 10 % differences in the mean precipitation rate for each  
 928 of the column-averaged condensation rates between the control-b and low-aerosol-b runs  
 929 (not shown). Figure 13 shows that generally a higher condensation rate is related to a higher  
 930 mean precipitation rate. It is also roughly shown that, according to the mean precipitation  
 931 rate for each condensation rate, overall, condensation rates below  $\sim 3 \times 10^{-3} \text{ g m}^{-3} \text{ s}^{-1}$  and  
 932 above  $\sim 10 \times 10^{-3} \text{ g m}^{-3} \text{ s}^{-1}$  are correlated with precipitation rates below  $\sim 2 \text{ mm hr}^{-1}$  and  
 933 above  $\sim 12 \text{ mm hr}^{-1}$ , respectively, while condensation rates between  $\sim 3$  and  $\sim 10 \times 10^{-3} \text{ g}$   
 934  $\text{m}^{-3} \text{ s}^{-1}$  are correlated with precipitation rates between  $\sim 2$  and  $\sim 12 \text{ mm hr}^{-1}$  (Figure 13).

**Deleted: 4**

**Deleted: 5**

**Deleted: 15**

**Deleted: 5**

**Deleted: 5**

935 Hence, on average, the higher frequency of condensation with rates above  $\sim 10 \times 10^{-3} \text{ g m}^{-3} \text{ s}^{-1}$  and below  $\sim 3 \times 10^{-3} \text{ g m}^{-3} \text{ s}^{-1}$  can be considered to lead to the higher frequency of  
 936 precipitation whose rates are higher than  $\sim 12 \text{ mm hr}^{-1}$  and lower than  $\sim 2 \text{ mm hr}^{-1}$  in the  
 937 control-b run, respectively. It can also be considered that the lower condensation frequency  
 938 between  $\sim 3$  and  $\sim 10 \times 10^{-3} \text{ g m}^{-3} \text{ s}^{-1}$  leads to the lower precipitation frequency between  $\sim 2$   
 939 and  $\sim 12 \text{ mm hr}^{-1}$  in the control-b run. It is found that this correspondence between  
 940 condensation and precipitation rates is valid whether analyses to construct Figure 13 are  
 941 repeated only for a time point at 16:30 LST or for a period between 16:30 and 17:00 LST.

**Deleted: 5**

953 These time point and period are related to analyses of the moist static energy as described  
 954 in Section e below.

955 At 17:20 LST, the larger precipitation frequency between  $\sim 2$  and  $\sim 12$   $\text{mm hr}^{-1}$  in the  
 956 low-aerosol-b run nearly offsets the larger precipitation frequency in the other ranges of  
 957 precipitation rates in the control-b run (Figure 9c). This leads to the similar average  
 958 precipitation rate between the runs at 17:20 LST and contributes to the similar cumulative  
 959 precipitation at the last time step between the runs (Figure 3b).

**Deleted: 11**

**Deleted: 5**

960

#### 961 **d. Evaporation and gust fronts**

962

963 As time progresses from 17:00 to 19:00 LST, the precipitation system moves northward  
 964 (Figure 14). At the core of the precipitation system, due to evaporation and downdrafts,  
 965 there is the horizontal outflow forming at 17:00 LST (Figures 14a and 14b). The core is  
 966 represented by the field of precipitation whose rates are higher than  $1 \text{ mm hr}^{-1}$  in Figure 14.  
 967 At the core, the northward outflow is magnified by the northward synoptic-scale wind,  
 968 while at the core, the outflow in the other directions is offset by the northward synoptic-  
 969 scale wind. Hence, the outflow is mainly northward from 17:00 LST onwards as marked  
 970 by yellow circles in Figures 14. This enables convergence or a gust front, which is produced  
 971 by the outflow from the core, to be mainly formed at the north of the core. Note that the  
 972 intensity of a gust front is proportional to that of outflow from a core of precipitation or  
 973 convective system (Weisman and Klemp, 1982; Houze, 1993). The strong gust front at the  
 974 north of the core generates strong updrafts, a significant amount of condensation and  
 975 precipitation. Then, a subsequent area with clouds and precipitation is formed at the north  
 976 of the core as time progresses, which means that the precipitation system extends or moves  
 977 to the north as seen in comparisons between sub-panels with different times in Figure 14.  
 978 This movement, which is induced by collaborative work between outflow, synoptic wind  
 979 and gust fronts, is typical in deep convective clouds.

**Deleted: 6**

**Deleted: 6**

**Deleted: 6**

**Deleted: 6**

**Deleted: 6**

**Deleted: 6**

980 As described above, the more droplet nucleation and greater integrated droplet surface  
 981 induce more condensation before 17:00 LST in the control-b run. This and lower efficiency  
 982 of collision and collection among droplets enable the control-b run to have a larger amount  
 983 of cloud liquid or droplets as a source of evaporation. This in turn enables more droplet

992 evaporation, more associated cooling and stronger downdrafts, although less rain  
 993 evaporation is in the control-b run particularly for the period from 17:00 LST to 19:00 LST.  
 994 The time- and domain-averaged droplet and rain evaporation rates are 0.72 (0.31) and 0.08  
 995 (0.13) g m<sup>-3</sup> h<sup>-1</sup>, respectively, while the time- and domain-averaged downdraft mass flux is  
 996 0.15 (0.10) kg m<sup>-2</sup> s<sup>-1</sup> over the period from 17:00 LST to 19:00 LST in the control-b (low-  
 997 aerosol-b) run. More evaporation of droplets and associated stronger downdrafts with  
 998 higher concentrations of aerosols acting as CCN have been shown by the numerous  
 999 previous studies (e.g., Tao et al., 2007; Tao et al., 2012; Khain et al., 2008; Lee et al., 2018).

**Deleted:** (Figure 17)

**Formatted:** Superscript  
**Formatted:** Superscript  
**Formatted:** Superscript  
**Formatted:** Superscript  
**Deleted:**

1000 During the period between 17:00 and 19:00 LST, with the development of convergence  
 1001 or the gust front, as mentioned above, the maximum precipitation rate increases from  $\sim 17$   
 1002 (17) to  $\sim 45$  (33) mm hr<sup>-1</sup> in the control-b (low-aerosol-b) run (Figure 9). This indicates  
 1003 that the gust-front development contributes to the overall intensification of the precipitation  
 1004 system, while it moves northward. If there were only northward synoptic-scale wind with  
 1005 no formation of the gust front, the system would move northward with less intensification.  
 1006 Over the period from 17:00 LST to 19:00 LST, stronger downdrafts and associated stronger  
 1007 outflow generate a stronger gust front and more subsequent condensation in the control-b  
 1008 run. This enhances the small initial difference, which is at 17:00 LST, in the frequency of  
 1009 precipitation with rates above  $\sim 12$  mm hr<sup>-1</sup> between the runs substantially as time  
 1010 progresses from 17:00 LST to 19:00 LST (Figure 9). Associated with this, with the time  
 1011 progress, the nearly identical maximum precipitation rate between the runs at 17:00 LST  
 1012 turns into the significantly higher maximum precipitation rate in the control-b run than in  
 1013 the low-aerosol-b run (Figure 9). Around 19:00 LST, the system enters its dissipating stage,  
 1014 accompanying reduction in the precipitating area and the area-averaged precipitation rate  
 1015 (Figures 3b).

**Deleted:** 11

**Deleted:** 11

**Deleted:** 11

**Deleted:** 5

**Deleted:** , 16m and 16n

**Deleted:**

#### 1017 e. Moist static energy

1018  
 1019 Condensation, which controls droplet mass and precipitation, is controlled by updrafts and  
 1020 updrafts are in turn controlled by instability. One of important factors that maintain  
 1021 instability is the moist static energy. Motivated by this, to better understand differences in  
 1022 the precipitation frequency distribution in association with those in the condensation

1031 frequency distribution between the control-b and low-aerosol-b runs, we calculate the flux  
 1032 of the moist static energy and the flux is defined as follows:

1033

1034  $\vec{F_S} = S \times \rho \times \vec{V}$  (1),

1035

1036 where  $\vec{F_S}$  represents the flux of the moist static energy,  $S$  the moist static energy,  $\rho$  the air  
 1037 density and  $\vec{V}$  the horizontal-wind vector. In Eq. (1), we see that the flux is in the vector  
 1038 form and has two components, which are its magnitude and direction. The fluxes of the  
 1039 moist static energy in the PBL are obtained over the domain at 16:30 LST, since in general,  
 1040 the moist static energy in the PBL has much stronger effects on instability and updrafts  
 1041 than that above the PBL. In particular, we focus on the PBL fluxes of the energy that cross  
 1042 the boundary over a time step at 16:30 LST between areas with the column-averaged  
 1043 condensation rate from  $3 \times 10^{-3} \text{ g m}^{-3} \text{ s}^{-1}$  to  $10 \times 10^{-3} \text{ g m}^{-3} \text{ s}^{-1}$ , which are referred to as “area  
 1044 A”, and those with the column-averaged condensation rate above  $10 \times 10^{-3} \text{ g m}^{-3} \text{ s}^{-1}$ , which  
 1045 are referred to as “area B”. This is because we are interested in the exchange of the moist  
 1046 static energy between areas A and B and this exchange can be seen by looking at those  
 1047 fluxes which cross the boundary between those areas.

1048 We are interested in the exchange of the energy, since we hypothesized that the  
 1049 exchange somehow alters instability in each of areas A and B in a way that there are  
 1050 increases (decreases) in instability, the updraft intensity, condensation and precipitation  
 1051 with increasing concentrations of aerosols acting as CCN in area B (A), leading to the  
 1052 higher (lower) frequency of condensation whose rates are higher than  $10 \times 10^{-3} \text{ g m}^{-3} \text{ s}^{-1}$   
 1053 (between  $3 \times 10^{-3}$  and  $10 \times 10^{-3} \text{ g m}^{-3} \text{ s}^{-1}$ ) and precipitation whose rates are higher than  $12$   
 1054  $\text{mm hr}^{-1}$  (between  $2$  and  $12 \text{ mm hr}^{-1}$ ) in the control-b run than in the low-aerosol-b run.  
 1055 When the PBL fluxes, which crosses the boundary over the time step at 16:30 LST, are  
 1056 summed at 16:30 LST, there is the net flux from area A to area B. This means that there is  
 1057 the net transportation of the moist static energy from areas with condensation rates between  
 1058  $3 \times 10^{-3}$  and  $10 \times 10^{-3} \text{ g m}^{-3} \text{ s}^{-1}$  to those with condensation rates greater than  $10 \times 10^{-3} \text{ g m}^{-3}$   
 1059  $\text{s}^{-1}$  in the PBL at 16:30 LST as shown in Table 2. Table 2 shows the net summed flux of the  
 1060 moist static energy which crosses the boundary between areas A and B in the control-b run  
 1061 as well as the low-aerosol-b run. To calculate the net flux at 16:30 LST in Table 2, the

1062 fluxes, which cross the boundary between areas A and B over the time step at 16:30 LST,  
 1063 only at grid points in the PBL are summed. For the calculation, the flux from area A to area  
 1064 B has a positive sign, while the flux from area B to area A has a negative sign. Since the  
 1065 net flux is positive for both of the runs as shown in Table 2, there is the net flux from area  
 1066 A to area B in the PBL. The above-described analysis for the fluxes crossing the boundary  
 1067 between areas A and B is repeated for every time step between 16:30 and 17:00 LST and  
 1068 based on this, the net summed flux over the period between 16:30 and 17:00 LST is  
 1069 obtained. As shown in Table 2, the net flux for the period between 16:30 and 17:00 LST is  
 1070 also positive as in the situation only for 16:30 LST. This means that there is the net  
 1071 transportation of the moist static energy from area A to area B in the PBL during the period  
 1072 between 16:30 and 17:00 LST.

1073 At 16:30 LST, condensation with rates above  $10 \times 10^{-3} \text{ g m}^{-3} \text{ s}^{-1}$  starts to develop and  
 1074 this forms area B. Area B has stronger updrafts via greater condensational heating than in  
 1075 other areas, including area A, with lower condensation rates. Stronger updrafts in area B  
 1076 induce the convergence of air and associated moist static energy from area A to area B.  
 1077 Since the average condensation rate and updrafts at 16:30 LST over area B are higher and  
 1078 stronger due to increasing concentrations of aerosols acting as CCN, respectively, the air  
 1079 convergence and the associated transportation of the moist static energy in the PBL from  
 1080 area A to area B are stronger and more, respectively, in the control-b run than in the low-  
 1081 aerosol-b run (Table 2). Stated differently, area B steals the moist static energy from area  
 1082 A, and this occurs more effectively in the control-b run. This increases instability and  
 1083 further intensifies updrafts in area B, and decreases instability and weakens updrafts in area  
 1084 A, while these increases and decreases (intensification and weakening) of instability  
 1085 (updrafts) are greater in the control-b run for the period from 16:30 LST to 17:00 LST.  
 1086 This increases condensation, cloud mass and precipitation whose rates are higher than 12  
 1087  $\text{mm hr}^{-1}$  in area B, and decreases condensation, cloud mass and precipitation whose rates  
 1088 are from 2  $\text{mm hr}^{-1}$  to 12  $\text{mm hr}^{-1}$  in area A. These increases and decreases occur more  
 1089 effectively for the control-b run than for the low-aerosol-b run during the period. This in  
 1090 turn leads to the lower precipitation frequency for the precipitation rates from 2  $\text{mm hr}^{-1}$  to  
 1091 12  $\text{mm hr}^{-1}$  and the higher frequency for the precipitation whose rates are higher than 12  
 1092  $\text{mm hr}^{-1}$  at 17:00 LST in the control-b run (Figure 2b). The weakened updrafts and reduced

Deleted: 11

1094 condensation turn a portion of precipitation with rates between 2 and 12 mm hr<sup>-1</sup> to  
 1095 precipitation whose rates are below 2 mm hr<sup>-1</sup>, and this takes place more efficiently in the  
 1096 control-b run during the period between 16:30 and 17:00 LST. This eventually increases  
 1097 the frequency of precipitation rates below 2 mm hr<sup>-1</sup> and this increase is greater for the  
 1098 control-b run, leading to the greater precipitation frequency for the precipitation rates  
 1099 below 2 mm hr<sup>-1</sup> in the control-b run at 17:20 LST (Figure 9c).

Deleted: 11

1100

## 1101 5. Discussion

1102

### 1103 5.1 Comparison of the Seoul and Beijing cases

1104

1105 In this section, we compare the Seoul case to the Beijing case. For the comparison,  
 1106 remember that on average, a pair of the control-s and low-aerosol-s runs has the same  
 1107 perturbation of aerosols acting as CCN as in a pair of the control-b and low-aerosol-b runs.  
 1108 Associated with the fact that clouds in the Seoul case are less deep than those in the Beijing  
 1109 case, overall, updrafts in the Seoul case are not as strong as those in the Beijing case. Hence,  
 1110 unlike the situation in the Beijing case, stronger updrafts, which accompany higher  
 1111 condensation rates, and associated convergence in the Seoul case are not strong enough to  
 1112 steal the sufficient amount of the moist static energy from weaker updrafts which  
 1113 accompany lower condensation rates. This makes the redistribution of the moist static  
 1114 energy between areas with relatively higher condensation rates and those with relative  
 1115 lower condensation rates, such as that between areas A and B for the Beijing case,  
 1116 ineffective for the Seoul case. Due to this, the sign of CCN-induced changes in the  
 1117 frequency of precipitation rates does not vary throughout all of the precipitation rates  
 1118 except for the range of low precipitation rates where there are nearly no CCN-induced  
 1119 changes in the frequency in the Seoul case as shown in Figure 4a. As seen in Figure 4a,  
 1120 mainly due to increases in condensation and deposition, precipitation frequency increases  
 1121 for most of precipitation rates, although the precipitation frequency does not show  
 1122 significant changes as concentration of aerosols acting as CCN increases for relatively low  
 1123 precipitation rates in the control-s run as compared to that in the low-aerosol-s run. This  
 1124 means that there are no tipping precipitation rates where the sign of CCN-induced changes

Deleted: 6

Deleted: 6

1128 in the frequency of precipitation rates changes in the Seoul case, contributing to the higher  
1129 cumulative precipitation amount in the simulation with higher concentrations of aerosols  
1130 acting as CCN for the Seoul case, which are different from the situation in the Beijing case.

1131 In the Beijing case with deeper clouds as compared to those in the Seoul case, clouds  
1132 develop gust fronts via strong downdrafts and associated strong outflow. These gust fronts  
1133 play an important role in developing strong convection and associated high precipitation  
1134 rates. Unlike the situation in the Seoul case, there are strong clouds and associated updraft  
1135 entities that are able to steal heat and moisture (or the moist static energy) as sources of  
1136 instability from areas with relatively less strong clouds and updrafts with medium strength;  
1137 note that these strong clouds here involve stronger updrafts via greater condensational  
1138 heating as described in Section e above and this enables these clouds to be thicker and have  
1139 higher cloud mass than these less strong clouds. This further intensifies strong clouds and  
1140 weakens less strong clouds with medium strength. Due to this, the cumulative frequency  
1141 of heavy (medium) precipitation in association with strong clouds (less strong clouds with  
1142 medium strength) increases (decreases). Some of the weakened clouds eventually produce  
1143 light precipitation, which increase the cumulative frequency for light precipitation. The  
1144 intensification of strong clouds and the weakening of less strong clouds with medium  
1145 strength gets more effective with increasing concentration of aerosols acting as CCN.  
1146 Hence, in the Beijing case, for medium precipitation in association with less strong clouds,  
1147 the simulation with higher concentration of aerosols acting as CCN shows the lower  
1148 cumulative precipitation frequency at the last time step. However, for heavy precipitation,  
1149 which is associated with strong clouds, and light precipitation, the simulation with higher  
1150 concentrations of aerosols acting as CCN shows the higher cumulative precipitation  
1151 frequency at the last time step. These differential responses of precipitation to increasing  
1152 concentration of aerosols acting as CCN among different types of precipitation occur in the  
1153 circumstances of the similar cumulative precipitation amount between the simulations with  
1154 different concentration of aerosols acting as CCN. This similar precipitation amount is due  
1155 to above-mentioned competition between CCN-induced changes in condensation,  
1156 deposition and freezing.

1157 In both of the Seoul and Beijing cases, CCN-induced changes in condensation plays an  
1158 important role in making differences in the precipitation amount and/or the precipitation

frequency distribution between the simulations with different concentration of aerosols acting as CCN. It is notable that in less deep clouds in the Seoul case, in addition to condensation, deposition plays a role in precipitation to induce CCN-induced increases in the precipitation amount. CCN-induced increases in condensation initiate the differences in cloud mass and precipitation and then CCN-induced increases in deposition follow to further enhance those differences. In deep clouds in the Beijing case, condensation tends to induce increases in cloud mass and precipitation, while deposition tends to induce decreases in cloud mass and precipitation with increasing concentration of aerosols acting as CCN. Hence, as clouds get shallower and thus ice processes become less active, the role of deposition in CCN-induced changes in precipitation amount turns from CCN-induced suppression of precipitation to enhancement of precipitation. Here, we find that contrary to the traditional understanding, the role of variation of freezing, which is induced by the varying concentration of aerosols acting as CCN but not INPs, in precipitation is negligible as compared to that of condensation and deposition in both of the cases.

1173

## 6. Summary and conclusions

1175

1176 This study examines impacts of aerosols, which act as CCN, on clouds and precipitation in  
1177 two metropolitan areas, which are the Seoul and Beijing areas, in East Asia that has  
1178 experienced substantial increases in aerosol concentrations over the last decades. The  
1179 examination is performed via simulations, which use a CSRM. These simulations are for  
1180 deep clouds which reach the tropopause in the Beijing case and for comparatively less deep  
1181 clouds which do not reach the tropopause yet grow above the level of freezing in the Seoul  
1182 case.

1183 In both of the cases, CCN-induced changes in condensation plays a critical role in  
1184 CCN-induced variation of precipitation properties (e.g., the precipitation amount and the  
1185 precipitation frequency distribution). In the Seoul case, CCN-induced increases in  
1186 condensation and subsequent increases in deposition lead to CCN-induced increases in the  
1187 precipitation frequency over most of precipitation rates and thus in the precipitation amount.  
1188 However, in the Beijing case, while there are increases in condensation with increasing  
1189 CCN concentrations, there are decreases in deposition with increasing CCN concentrations.

1190 This competition between increases in condensation and decreases in deposition leads to  
1191 negligible CCN-induced changes in cumulative precipitation amount in the Beijing case.  
1192 In both of the cases, CCN-induced changes in freezing are negligible as compared to those  
1193 in condensation and deposition. In the Beijing case, there is another competition for the  
1194 moist static energy among clouds with different updrafts and condensation. This  
1195 competition results in CCN-induced differential changes in the precipitation frequency  
1196 distributions. With clouds getting deeper from the Seoul case to the Beijing case, clouds  
1197 and associated updrafts, which are strong enough to steal the moist static energy from other  
1198 clouds and their updrafts, appear. This makes strong clouds stronger and clouds with  
1199 medium strength weaker. With higher CCN concentrations, strong clouds steal more  
1200 energy, and thus strong clouds become stronger and clouds with medium strength weaker  
1201 with a greater magnitude. As a result of this, there are more frequent heavy precipitation  
1202 (whose rates are higher than  $12 \text{ mm hr}^{-1}$ ) and light precipitation (whose rates are lower than  
1203  $2 \text{ mm hr}^{-1}$ ), and less frequent medium precipitation (with rates from  $2 \text{ mm hr}^{-1}$  to  $12 \text{ mm hr}^{-1}$ )  
1204 with increasing CCN concentrations in the Beijing case.

1205 In both of the Seoul and Beijing cases, there are mountains and they play an important  
1206 role in how cloud and precipitation evolve with time and space. In both of the cases, the  
1207 precipitating system moves or expands over mountains which induce forced convection  
1208 and generate condensation. This important role of mountains and forced convection in the  
1209 formation and evolution of the precipitation system has not been examined much in the  
1210 previous studies of aerosol-cloud interactions, since many of those previous studies (e.g.,  
1211 Jiang et al., 2006; Khain et al., 2008; Li et al., 2011; Morrison et al., 2011) have dealt with  
1212 convective clouds that develop over plains and oceans. Hence, findings in this study, which  
1213 are related to mountain-forced convection and its interactions with aerosols, can be  
1214 complementary to those previous studies. Stated differently, this study can shed light on  
1215 our path to the understanding of aerosol-cloud interactions over more general domains not  
1216 only with no terrain but also with terrain.

1217

1218

1219

1220

1221 **Code/Data source and availability**

1222

1223 Our private computer system stores the code/data which are private and used in this study.

1224 Note that in particular, the stored PM data are provided by the Korea Environment  
1225 Cooperation in South Korea and State Key Laboratory of Severe Weather in China. Upon  
1226 approval from funding sources, the data will be opened to the public. Projects related to  
1227 this paper have not been finished, thus, the sources prevent the data from being open to the  
1228 public currently. However, if information on the data is needed, contact the corresponding  
1229 author Seoung Soo Lee (slee1247@umd.edu).

1230

1231 **Author contributions**1232 Essential initiative ideas are provided by SSL, KJH and KHS to start this work. Simulation  
1233 and observation data are analyzed by SSL, JC and GK. JU and YZ review the results and  
1234 contributeto their improvement. CHJ and JG perform additional simulations, which are  
1235 required by the review process, and their basic analyses. CHJ and SKS, provide ideas to  
1236 handle the reviewers' comments.

1237

1238 **Competing interests**

1239 The authors declare that they have no conflict of interest.

1240

1241 **Acknowledgements**1242 This study is supported by the National Research Foundation of Korea (NRF) grant funded  
1243 by the Korea government (MSIT) (No. NRF2020R1A2C1003215) and the "Construction  
1244 of Ocean Research Stations and their Application Studies" project funded by the Ministry  
1245 of Oceans and Fisheries, South Korea. This study is also supported by the National  
1246 Research Foundation of Korea (NRF) by FRIEND (Fine Particle Research Initiative in East  
1247 Asia Considering National Differences) project through the National Research Foundation  
1248 of Korea (NRF) funded by the Ministry of Science and ICT (2020M3G1A1114617), and  
1249 the Korea Meteorological Administration Research and Development Program "Research  
1250 on Weather Modification and Cloud Physics" under Grant (KMA2018-00224). Authors  
1251 thank Danhong Dong at Chinese Academy of Sciences and Fang Wu at Beijing Normal  
1252 University for their reviewing this paper.

Formatted: Font: (Default) Batang, (Asian) Batang

Deleted: also

Deleted: .

Deleted: 1

1255 **References**

1256

1257 Brown, A., Milton, S., Cullen, M., Golding, B., Mitchell, J., and Shelly, A.: Unified  
1258 modeling and prediction of weather and climate: A 25-year journey, *Bull. Am  
1259 Meteorol. Soc.* 93, 1865–1877, 2012.

1260 Chen, F., and Dudhia, J.: Coupling an advanced land-surface hydrology model with the  
1261 Penn State-NCAR MM5 modeling system. Part I: Model description and  
1262 implementation, *Mon. Wea. Rev.*, 129, 569–585, 2001.

1263 Dong, B., Wilcox, L. J., Highwood, E. J., and Sutton, R. T.: Impacts of recent decadal  
1264 changes in Asian aerosols on the East Asian summer monsoon: roles of aerosol–  
1265 radiation and aerosol–cloud interactions, *Clim. Dyn.*, 53, 3235–3256, 2019.

1266 Eun, S.-H., Kim, B.-G., Lee, K.-M., and Park, J.-S.: Characteristics of recent severe haze  
1267 events in Korea and possible inadvertent weather modification, *SOLA*, 12, 32–36,  
1268 2016.

1269 Fan, J., Yuan, T., Comstock, J. M., et al.: Dominant role by vertical wind shear in regulating  
1270 aerosol effects on deep convective clouds, *J. Geophys. Res.*, 114,  
1271 doi:10.1029/2009JD012352, 2009.

1272 Fouquart, Y., and Bonnel, B.: Computation of solar heating of the Earth's atmosphere: a  
1273 new parameterization, *Beitr. Phys. Atmos.*, 53, 35–62, 1980.

1274 Ha, K.-J., Nam, S., Jeong, J.-Y., et al., Observations utilizing Korean ocean research  
1275 stations and their applications for process studies, *Bull. Amer. Meteor. Soc.*, 100,  
1276 2061–2075, 2019.

1277 Holben, B. N., Tanré, D., Smirnov, et al.: An emerging ground-based aerosol climatology:  
1278 Aerosol optical depth from AERONET, *J. Geophys. Res.*, 106, 12067–12097, 2001.

1279 Houze, R. A., Cloud dynamics, Academic Press, 573 pp, 1993.

1280 Hwang, S.-O., and Lee, D.-K.: A study on the relationship between heavy rainfalls and  
1281 associated low-level jets in the Korean peninsula, *J. Korean. Meteorol. Soc.*, 29, 133–  
1282 146, 1993.

1283 Jiang, H., Xue, H., Teller, A., Feingold, G., and Levin, Z.: Aerosol effects on the lifetime  
1284 of shallow cumulus, *Geophys. Res. Lett.*, 33, L14806, doi:10.1029/2006GL026024,  
1285 2006.

1290 Kar, S. K., Lioi, Y.A., and Ha, K.-J. : Aerosol effects on the enhancement of cloud-to-  
1291 ground lightning over major urban areas of South Korea, *Atmos. Res.* , 92, 80-87,  
1292 2009.

1293 Khain, A., BenMoshe, N., and Pokrovsky, A.: Factors determining the impact of aerosols  
1294 on surface precipitation from clouds: Attempt of classification, *J. Atmos. Sci.*, 65,  
1295 1721-1748, 2008.

1296 Khain, A., Pokrovsky, A., Rosenfeld, D., Blahak, U., and Ryzhkov, A.: The role of CCN in  
1297 precipitation and hail in a mid-latitude storm as seen in simulations using a spectral  
1298 (bin) microphysics model in a 2D dynamic frame, *Atmos. Res.*, 99, 129–146, 2011.

1299 Khain, A., Rosenfeld, D., and Pokrovsky, A.: Aerosol impact on the dynamics and  
1300 microphysics of deep convective clouds, *Quart. J. Roy. Meteor. Soc.*, 131, 2639-266,  
1301 2005.

1302 Khain, A. D., BenMoshe, N., and A. Pokrovsky, A.: Factors determining the impact of  
1303 aerosols on surface precipitation from clouds: An attempt at classification, *J. Atmos.*  
1304 *Sci.*, 65, 1721–1748, doi:10.1175/2007JAS2515.1, 2008.

1305 King, J.: Automatic weather stations, available at  
1306 <https://web.archive.org/web/20090522121225/http://www.automaticweatherstation.com/index.html>, 2009.

1308 Koop, T., Luo, B. P., Tsias, A., and Peter, T.: Water activity as the determinant for  
1309 homogeneous ice nucleation in aqueous solutions, *Nature*, 406, 611-614, 2000.

1310 Lebo, Z. J., and Morrison, H.: Dynamical effects of aerosol perturbations on simulated  
1311 idealized squall lines, *Mon. Wea. Rev.*, 142, 991-1009, 2014.

1312 Lee, D.-K., Kim, H.-R., and Hong, S.-Y.: Heavy rainfall over Korea during 1980–1990.  
1313 *Korean J. Atmos. Sci.*, 1, 32–50, 1998.

1314 Lee, S., Ho, C.-H., Lee, Y. G., Choi, H.-J. and Song, C.-K.: Influence of transboundary air  
1315 pollutants from China on the high-PM10 episode in Seoul, Korea for the period  
1316 October 16–20, 2008. *Atmos. Environ.*, 77, 430–439, 2013.

1317 Lee, S. S., Donner, L. J., Phillips, V. T. J., and Ming, Y.: The dependence of aerosol effects  
1318 on clouds and precipitation on cloud-system organization, shear and stability, *J.*  
1319 *Geophys. Res.*, 113, D16202, 2008.

1320 Lee, S. S., Kim, B.-G., and Yum, S. S., et al.: Effect of aerosol on evaporation, freezing and

1321 precipitation in a multiple cloud system, *Clim. Dyn.*, 48, 1069-1087, 2016.

1322 Lee, S. S., Li, Z., Mok, J., et al.: Interactions between aerosol absorption, thermodynamics,  
1323 dynamics, and microphysics and their impacts on clouds and precipitation in a  
1324 multiple-cloud system, *Clim. Dyn.*, <https://doi.org/10.1007/s00382-017-3552-x>,  
1325 2017.

1326 Lee, S. S., Kim, B.-G., Li, Z., Choi, Y.-S., Jung, C.-H., Um, J., Mok, J., and Seo, K.-H.:  
1327 Aerosol as a potential factor to control the increasing torrential rain events in urban  
1328 areas over the last decades, *Atmos. Chem. Phys.*, 18, 12531–12550,  
1329 <https://doi.org/10.5194/acp-18-12531-2018>, 2018.

1330 Li, Z., Niu, F., Fan, J., Liu, Y., Rosenfeld, D., and Ding, Y.: Long-term impacts of aerosols  
1331 on the vertical development of clouds and precipitation, *Nat. Geosci.*, 4, 888-894,  
1332 2011.

1333 Lohmann, U. and Diehl, K.: Sensitivity studies of the importance of dust ice nuclei for the  
1334 indirect aerosol effect on stratiform mixed-phase clouds, *J. Atmos. Sci.*, 63, 968-982,  
1335 2006.

1336 Lu, Z., Zhang, Q., and Streets, D. G.: Sulfur dioxide and primary carbonaceous aerosol  
1337 emissions in China and India, 1996–2010, *Atmos. Chem. Phys.*, 11, 9839–9864, 2011.

1338 Mlawer, E. J., Taubman, S. J., Brown, P. D., Iacono, M. J., and Clough, S. A.: RRTM, a  
1339 validated correlated-k model for the longwave, *J. Geophys. Res.*, 102, 16663-1668,  
1340 1997.

1341 Möhler, O., et al, Efficiency of the deposition mode ice nucleation on mineral dust particles,  
1342 *Atmos. Chem. Phys.*, 6, 3007-3021, 2006.

1343 Morrison, H., and Grabowski, W. W.: Cloud-system resolving model simulations of aerosol  
1344 indirect effects on tropical deep convection and its thermodynamic environment,  
1345 *Atmos. Chem. Phys.*, 11, 10503–10523, 2011.

1346 Oh, H., Ha, K.-J. and Timmermann, A.: Disentangling Impacts of Dynamic and  
1347 Thermodynamic Components on Late Summer Rainfall Anomalies in East Asia, *J.*  
1348 *Geophys. Res.*, 123, 8623-8633, 2018.

1349 Oh, H.-R., Ho, C.-H., Kim, J., Chen, D., Lee, S., Choi, Y.-S., Chang, L.-S., and Song, C.-  
1350 K.: Long-range transport of air pollutants originating in China: A possible major cause  
1351 of multi-day high-PM10 episodes during cold season in Seoul, Korea. *Atmos.*

1352 Environ., 109, 23–30, 2015.

1353 Pruppacher, H. R. and Klett, J. D.: Microphysics of clouds and precipitation, 714pp, D.

1354 Reidel, 1978.

1355 Rosenfeld, D., Lohmann, U., Raga, G. B., et al.: Flood or drought, How do aerosols affect

1356 precipitation? *Science*, 321, 1309-1313, 2008.

1357 Storer, R. L., van den Heever, S. C., and Stephens, G. L.: Modeling aerosol impacts on

1358 convection under differing storm environments, *J. Atmos. Sci.*, 67, 3904-3915, 2010.

1359 Seo, K.-H., Son, J. H., Lee, J.-H., and Park, H.-S.: Northern East Asian monsoon

1360 precipitation revealed by air mass variability and its prediction, *J. Clim.*, 28, 6221-

1361 6233, 2013.

1362 Tao, W.-K., Chen, J.-P., Li, Z., Wang, C., and Zhang, C.: Impact of aerosols on convective

1363 clouds and precipitation, *Rev. Geophys.*, 50, RG2001, 2012.

1364 Tao, W. K., Cloud resolving modeling, *J. Meteorol. Soc. Jpn.*, 85B, 305–330,

1365 doi:10.2151/jmsj.85B.305, 2007.

1366 van den Heever, S. C., Carrió, G. G., Cotton, W. R., DeMott, P. J., and Prenni, A. J.:

1367 Impacts of nucleating aerosol on Florida storms. part I: Mesoscale simulations, *J.*

1368 *Atmos. Sci.*, 63, 1752–1775, 2006.

1369 Wang, H., Skamarock, W. C., and Feingold, G.: Evaluation of scalar advection schemes in

1370 the Advanced Research WRF model using large-eddy simulations of aerosol-cloud

1371 interactions, *Mon. Wea. Rev.*, 137, 2547-2558, 2009.

1372 Weisman, M. L., and Klemp, J. B.: The dependence of numerically simulated convective

1373 storms on vertical wind shear and buoyancy, *Mon. Wea. Rev.*, 110, 504-520, 1982.

1374

1375

1376

1377

1378

1379

1380

1381

1382

1383

1384

1385

1386

1387 **FIGURE CAPTIONS**

1388

1389 Figure 1. Inner rectangles in (a) and (b) mark the Seoul area in the Korean Peninsula and  
 1390 the Beijing area in the East-Asia continent, respectively. A dot outside the inner rectangle  
 1391 in (a) marks Baekryongdo island. Dots in the inner rectangles in (a) and (b) mark the  
 1392 selected locations where precipitation and aerosol mass are measured. In (a) and (b), the  
 1393 light blue represents the ocean and the green the land area.

1394

1395 Figure 2. Time series of PM<sub>2.5</sub> observed at the ground station in Baekryongdo island (blue  
 1396 line) and of the average PM<sub>2.5</sub> over ground stations in the Seoul area (red line) between  
 1397 07:00 LST on December 22<sup>nd</sup> and 21:00 LST on December 24<sup>th</sup> in 2017. Note that PM<sub>2.5</sub>  
 1398 observed at stations in the Seoul area is applied to the control-s run whose period is marked  
 1399 by the dashed rectangle. Time series of the average PM<sub>2.5</sub> over stations in the Seoul area in  
 1400 the low-aerosol-s run for the simulation period is also shown (black solid line).

1401

1402 Figure 3. Time series of precipitation rates at the surface, which are averaged over the  
 1403 domain and smoothed over 1 hour, (a) for the control-s and low-aerosol-s runs in the Seoul  
 1404 area and (b) for the control-b and low-aerosol-b runs in the Beijing area. In (a) and (b), the  
 1405 averaged and observed precipitation rates over the observation sites in the Seoul and  
 1406 Beijing areas, respectively, are also shown.

1407

1408 Figure 4. Observed and simulated cumulative frequency distributions of precipitation rates  
 1409 at the surface for (a) the Seoul case, which are collected over the Seoul area, and (b) the  
 1410 Beijing case, which are collected over the Beijing area, at the last time step. Simulated  
 1411 distributions are in the control-s and low-aerosol-s runs for the Seoul case and in the  
 1412 control-b and low-aerosol-b runs for the Beijing case. The observed distribution is obtained  
 1413 by interpolating and extrapolating the observed precipitation rates to grid points and time  
 1414 steps in the control-s and control-b runs for the Seoul and Beijing cases, respectively.

1415

**Deleted:** 1

**Deleted:** Figure 1. Wind ( $m s^{-1}$ ), equivalent potential temperature (K), and geopotential height (m) at 850 hPa level over Northeast Asia at (a) 21:00 LST December 23<sup>rd</sup> 2017 and (b) 09:00 LST July 27<sup>th</sup> 2015. Wind, equivalent potential temperature, and geopotential height are represented by arrows, a shaded field, and contours, respectively. An inner rectangle in the Korean Peninsula in (a) marks the Seoul area and that in the East-Asia continent in (b) marks the Beijing area. 1

**Deleted:** 2

**Deleted:** Figure 3. Surface size distribution of aerosols (a) for the Seoul case and (b) for the Beijing case. Aerosol number concentration per unit volume of air is represented by N and aerosol diameter by D. 1

**Deleted:** 4

**Deleted:** 5

**Deleted:** 6

1435 Figure 5. Cumulative frequency distributions of the precipitation rates at the surface in the  
 1436 control-s and low-aerosol-s runs for the Seoul case at (a) 06:00, (b) 10:00 and (c) 12:00  
 1437 LST.

**Deleted: 7**

1438  
 1439 Figure 6. Vertical distributions of differences in the area-averaged condensation,  
 1440 deposition and freezing rates, and cloud-liquid, raindrop, snow and hail mass density, and  
 1441 updraft mass fluxes between the control-s and low-aerosol-s runs at (a) 03:20, (b) 03:40,  
 1442 (c) 06:00 and (d) 12:00 LST. The horizontal black line in each panel represents the altitude  
 1443 of freezing or melting. Here, for the sake of the display brevity, snow mass density includes  
 1444 ice-mass density, while hail mass density includes graupel mass density.

**Deleted: 8**

1445  
 1446 Figure 7. Spatial distributions of terrain heights, column-averaged condensation rates,  
 1447 surface wind vectors and precipitation rates at (a) and (b) 03:40, (c) and (d) 08:40, (e) and  
 1448 (f) 10:00, and (g) and (h) 12:00 LST. The distributions in the control-s run are shown in (a),  
 1449 (c), (e) and (g), and the distributions in the low-aerosol-s run are shown in (b), (d), (f) and  
 1450 (h). Condensation rates are shaded. Dark-yellow and dark-red contours represent  
 1451 precipitation rates at 0.5 and 3.0  $\text{mm hr}^{-1}$ , respectively, while beige, light brown and brown  
 1452 contours represent terrain heights at 100, 300 and 600 m, respectively. See text for yellow  
 1453 rectangles in (a), (b), (c) and (d).

**Deleted: 9**

**Deleted: 7**

**Deleted: 2**

**Deleted: 08**

**Deleted: 4**

**Deleted: (g) and (h) 10:00, (i) and (j) 11:00,**

**Deleted: k**

**Deleted: l**

**Deleted: ,**

**Deleted: (g), (i)**

**Deleted: k**

**Deleted: ,**

**Deleted: (j) and (l)**

**Deleted: g**

**Deleted: h**

**Deleted: 10**

**Deleted: 11**

1454  
 1455 Figure 8. Cumulative frequency distributions of the column-averaged condensation rates  
 1456 in the control-s and low-aerosol-s runs for the Seoul case at (a) 07:20 and (b) 09:00 LST.

**Deleted: 2**

**Deleted: 8**

1457  
 1458 Figure 9. Cumulative frequency distributions of the precipitation rates at the surface in the  
 1459 control-b and low-aerosol-b runs for the Beijing case at (a) 16:00, (b) 17:00, (c) 17:20, and  
 1460 (d) 19:00 LST.

1461

1462 Figure 10. Same as Figure 6 but for differences between the control-b and low-aerosol-b  
 1463 runs at (a) 14:20, (b) 15:40, (c) 16:00, (d) 17:20 and (e) 19:00 LST.

1464

1486 Figure 11. Spatial distributions of terrain heights, column-averaged condensation rates,  
 1487 surface wind vectors and precipitation rates at (a) and (b) 14:20, and (c) and (d) 17:20 LST.  
 1488 (a) and (c) are for the control-b run and (b) and (d) are for the low-aerosol-b run.  
 1489 Condensation rates are shaded. Dark-yellow and dark-red contours represent precipitation  
 1490 rates at 1.0 and 2.0  $\text{mm hr}^{-1}$ , respectively, while beige, light brown, brown and dark brown  
 1491 contours represent terrain heights at 100, 500, 1000 and 1500 m, respectively. See text for  
 1492 yellow circles in (a) and (b).

1493

1494 Figure 12. Cumulative frequency distributions of the column-averaged condensation rates  
 1495 in the control-b and low-aerosol-b runs for the Beijing case at (a) 17:20 and (b) 19:00 LST.

1496

1497 Figure 13. Mean precipitation rates corresponding to each column-averaged condensation  
 1498 rate for the period between 14:00 and 17:20 LST in the control-b run. One standard  
 1499 deviation of precipitation rates is represented by a vertical bar at each condensation rate.

1500

1501 Figure 14. Spatial distributions of precipitation rates (shaded) and wind vectors (arrows)  
 1502 for the Beijing case at (a) and (b) 17:00, ~~and (c) and (d) 19:00~~. The distributions in the  
 1503 control-b run are in (a) ~~and (c)~~. The distributions in the low-aerosol-b run are in (b) ~~and (d)~~.

1504

1505

1506

1507

1508

1509

1510

1511

1512

1513

1514

1515

Deleted: 3

Deleted: 4

Deleted: 5

Deleted: 6

Deleted: (c) and (d) 17:20, (e) and (f) 17:40,

Deleted: g

Deleted: )

Deleted: h

Deleted: 8

Deleted: , (i) and (j) 18:20, (k) and (l) 18:40, and (m) and (n) 19:00 LST

Deleted: , (c), (e)

Deleted: ,

Deleted: g

Deleted: , (i), (k) and (m)

Deleted: ,

Deleted: , (f), (h), (j), (l) and (n)

Deleted: Figure 17. Vertical distributions of (a) the area-averaged  
 cloud-liquid and rain evaporation rates and (b) downdraft mass  
 fluxes in the control-b and low-aerosol-b runs over a period from  
 17:00 to 19:00 LST.

Deleted: 1

Simulations	Site	Concentrations of background aerosols acting as CCN
Control-s run	Seoul area	Observed and affected by the aerosol advection
Low-aerosol-s run	Seoul area	Same as those in the control-s run but unaffected by the aerosol advection
Control-b run	Beijing area	Observed
Low-aerosol-b run	Beijing area	Reduced by a factor of 3.1 as compared to those observed

1563

1564 Table 1. Summary of simulations

1565

1566

Simulations	The net flux of the moist static energy which crosses the boundary between areas A and B ( $\text{J m}^{-2} \text{s}^{-1}$ )	
	At 16:30 LST	16:30 to 17:00 LST
Control-b run	$1.57 \times 10^{12}$	$1.07 \times 10^{15}$
Low-aerosol-b run	$1.15 \times 10^{12}$	$7.55 \times 10^{14}$

1567

1568 Table 2. The net flux of the moist static energy which crosses the boundary between areas  
1569 A and B at 16:30 LST and for a period from 16:30 to 17:00 LST.

1570

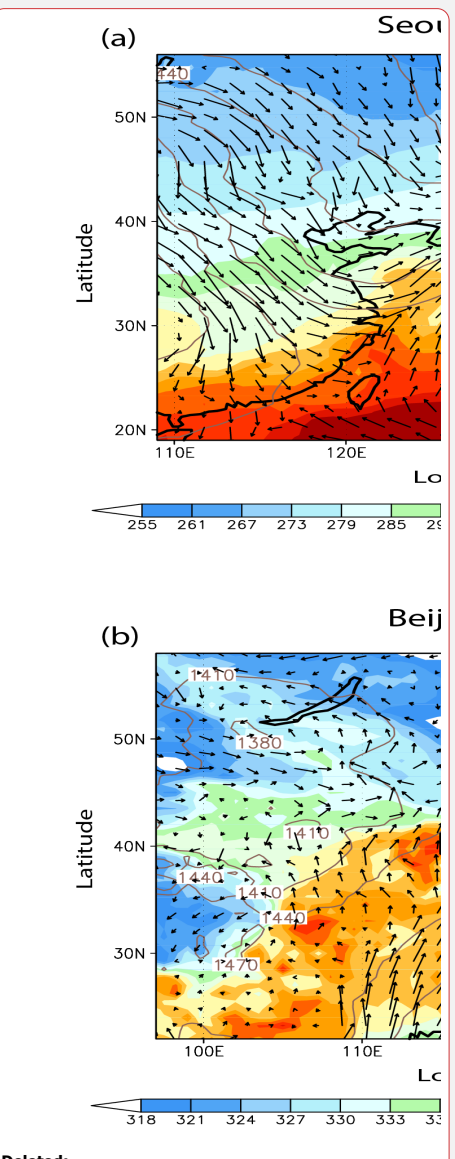
1571

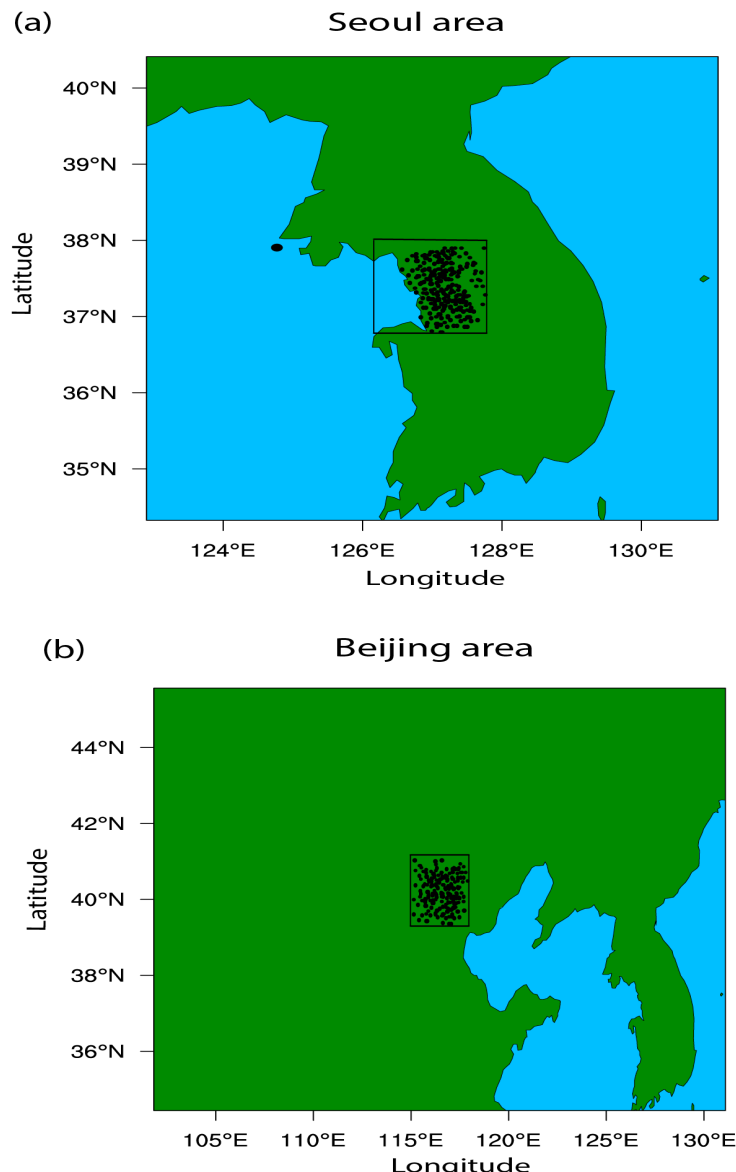
1572

1573

1574

1575

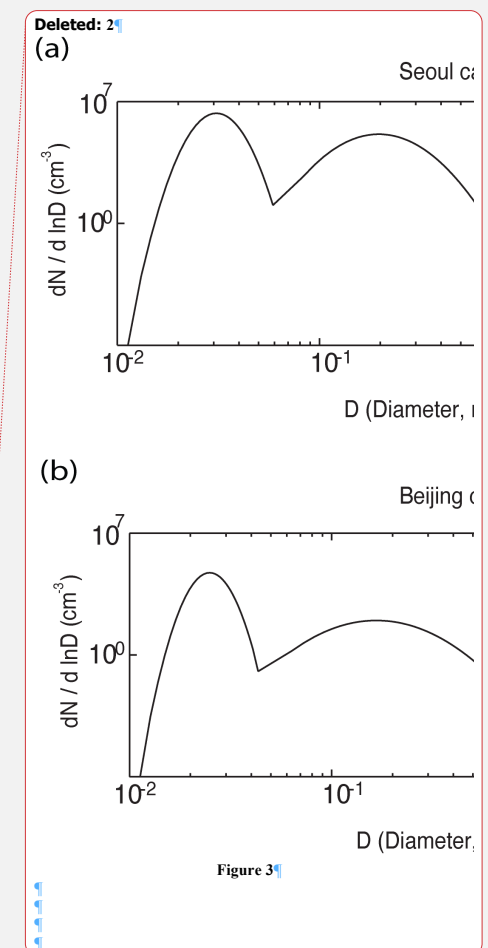




1578

1579

Figure 1



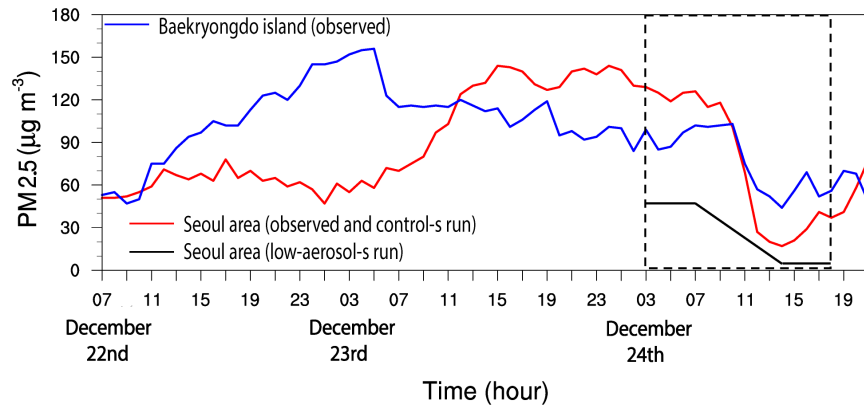


Figure 2

Deleted: 4

1587

1588

1589

1590

1591

1592

1593

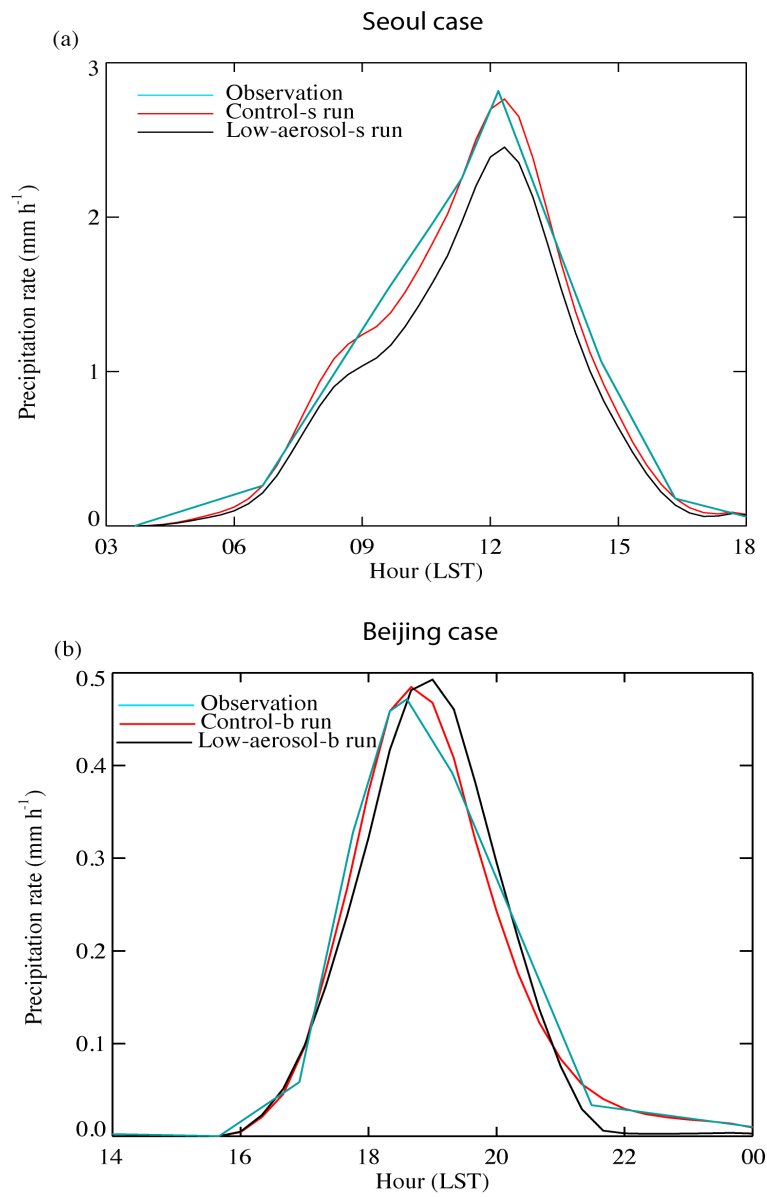
1594

1595

1596

1597

1598

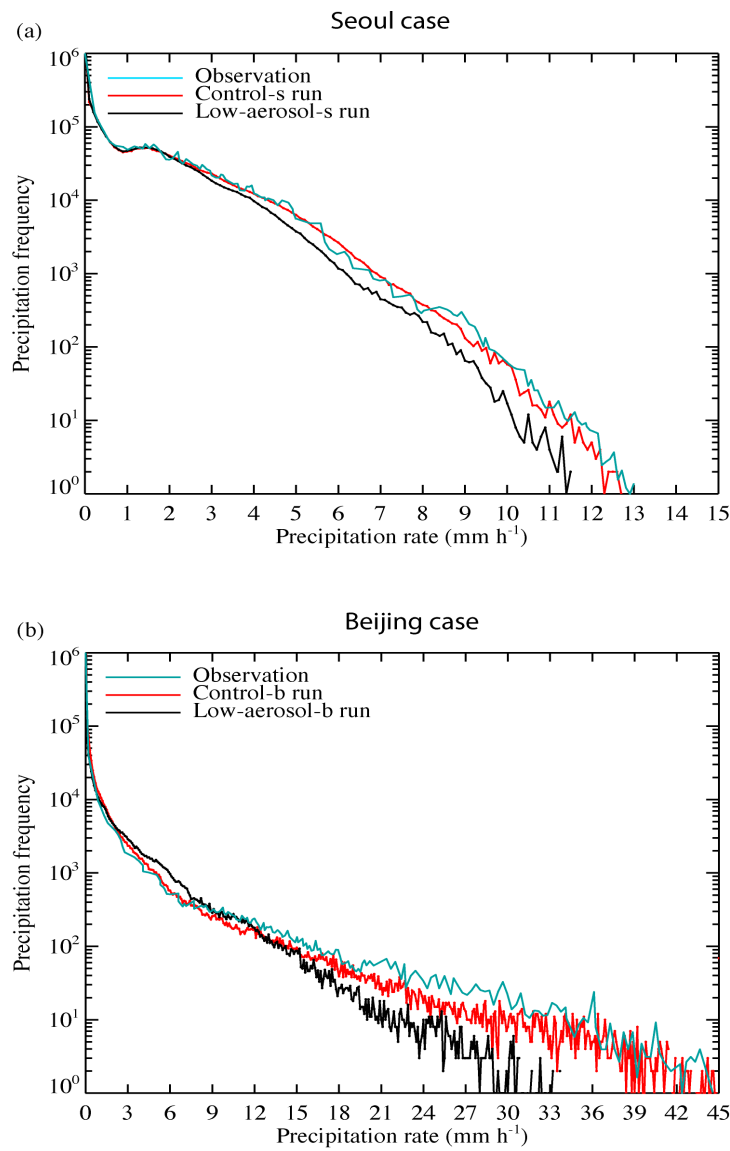


1600

1601

**Figure 3**

Deleted: 5



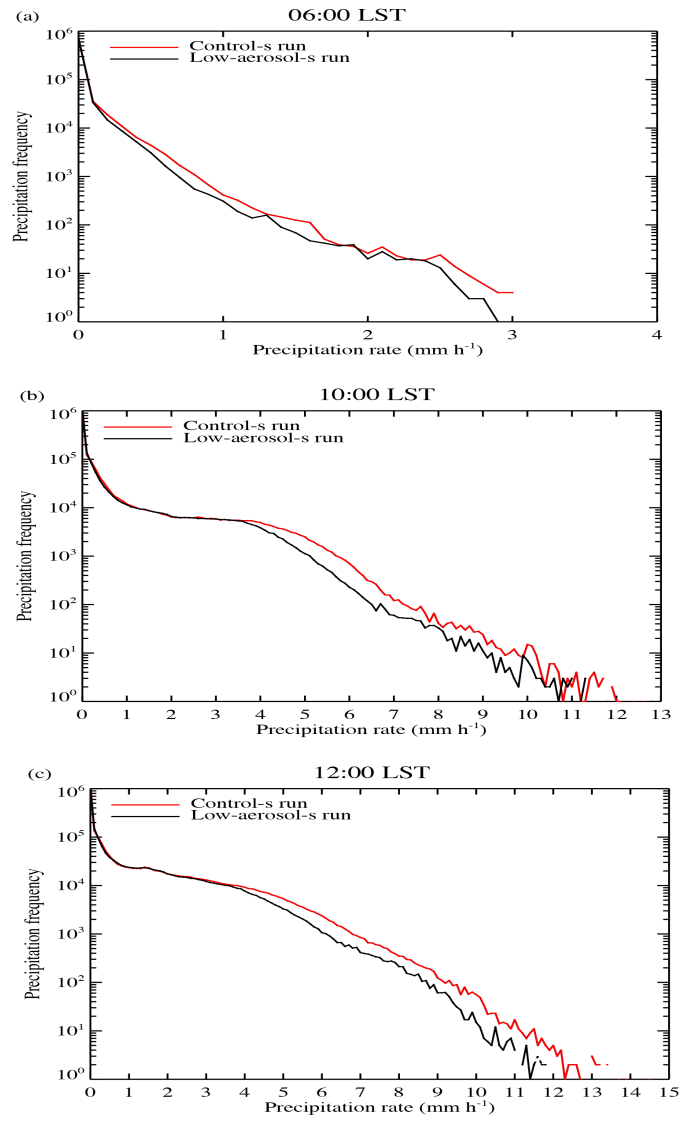
1603

1604

Figure 4

Deleted: 6

### Seoul case



1606

1607

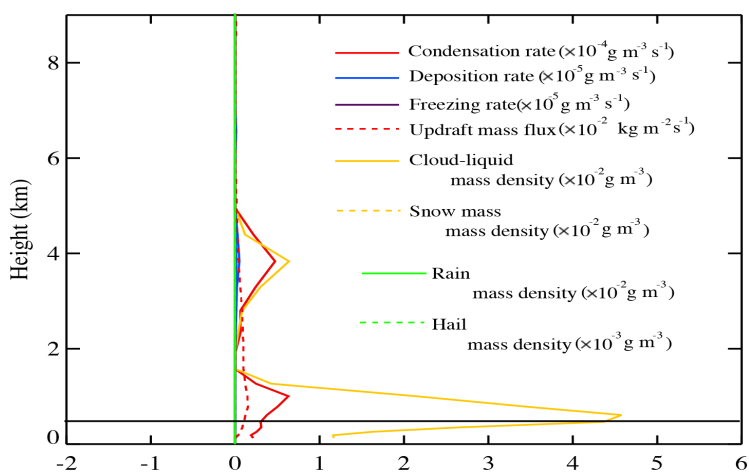
Figure 5

Deleted: 7

**Seoul case**  
**(control-s run minus low-aerosol-s run)**

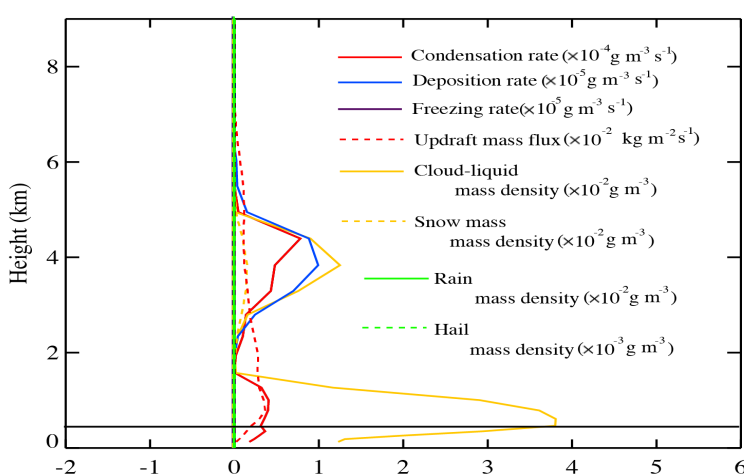
(a)

03:20 LST



(b)

03:40 LST

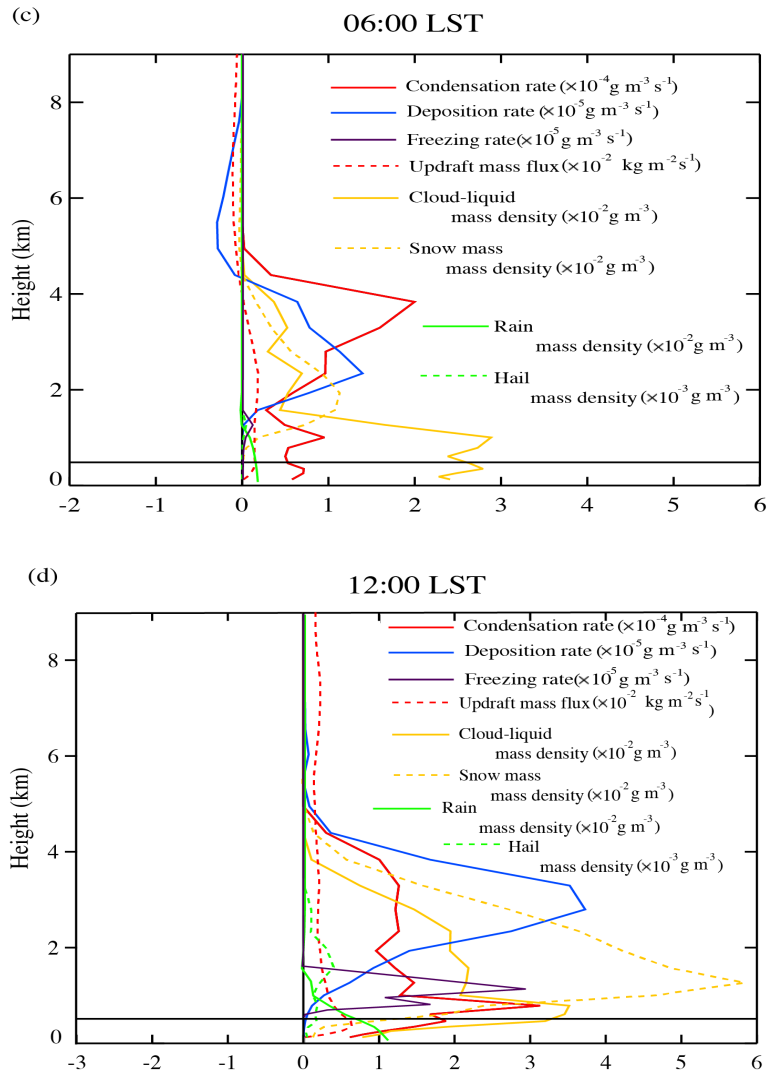


1609

1610

**Figure 6**

Deleted: 8



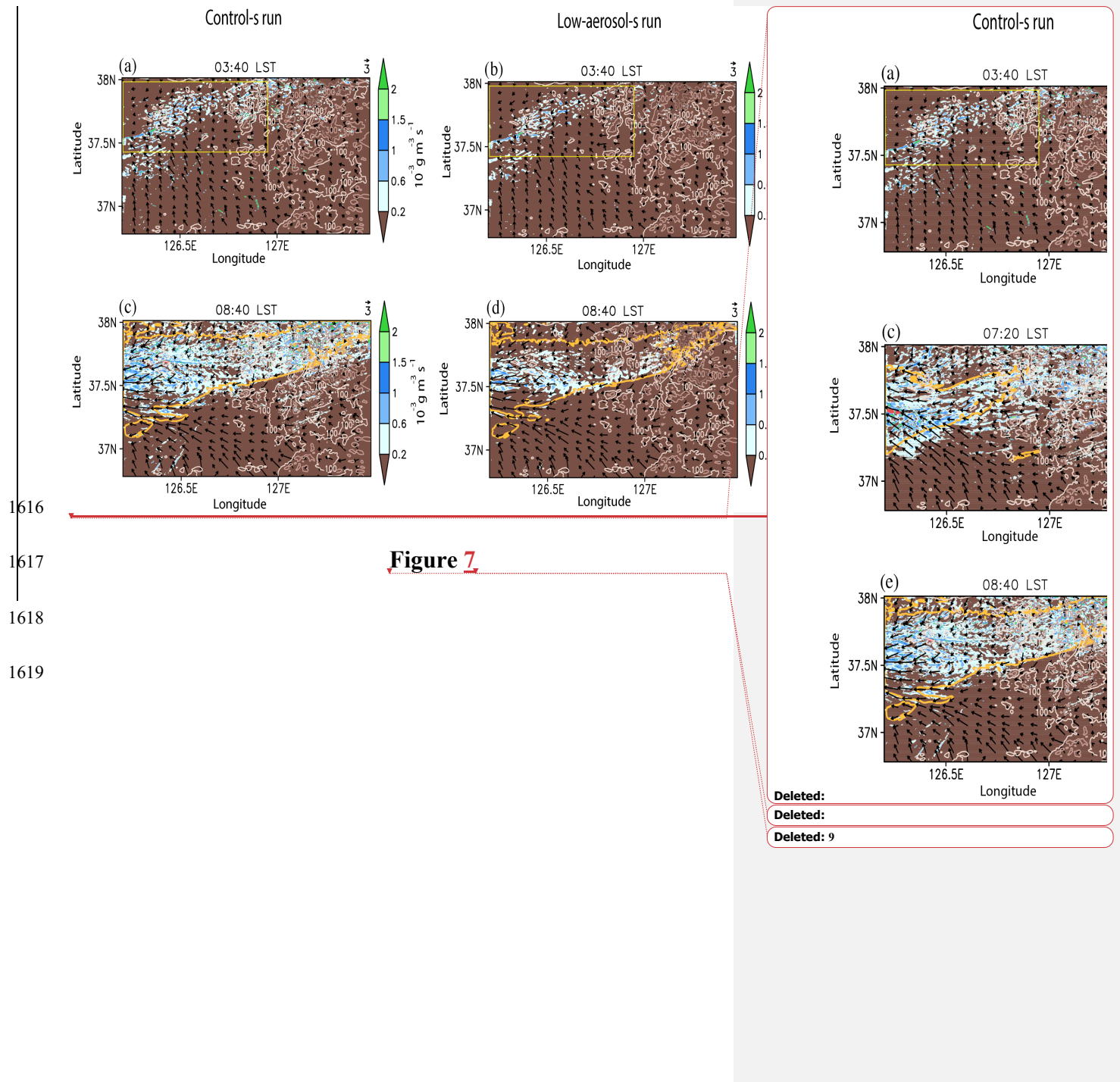
1612

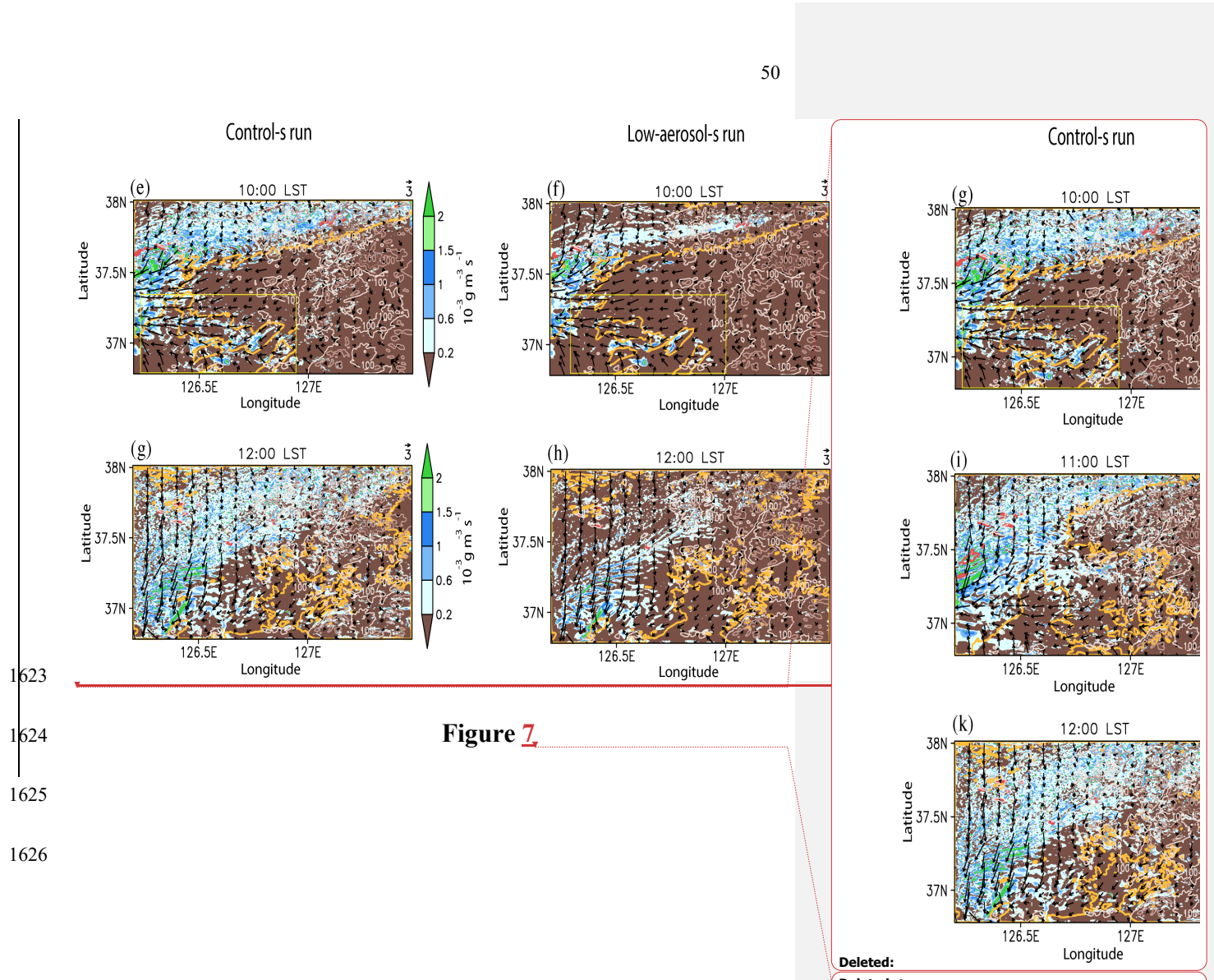
1613

1614

Figure 6

**Deleted: 8**

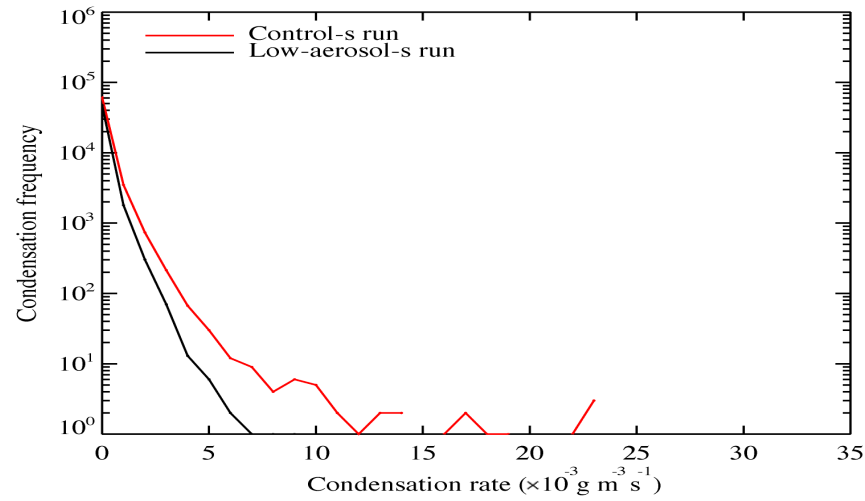




### Seoul case

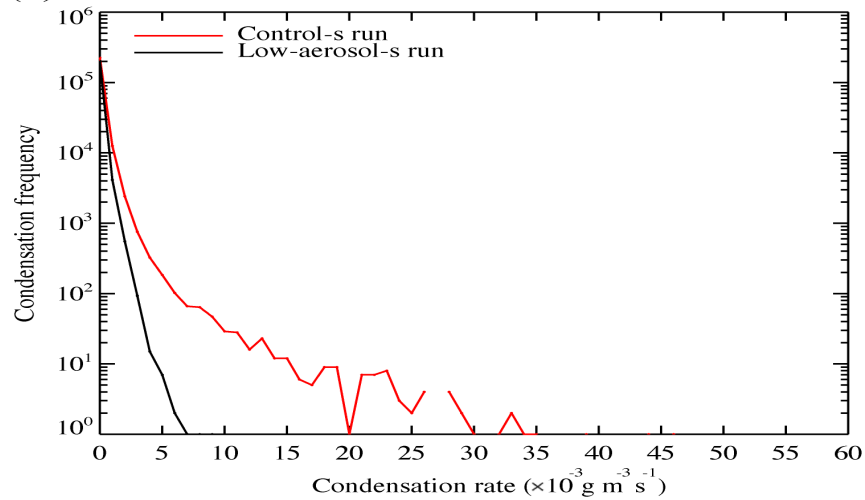
(a)

07:20 LST



(b)

09:00 LST



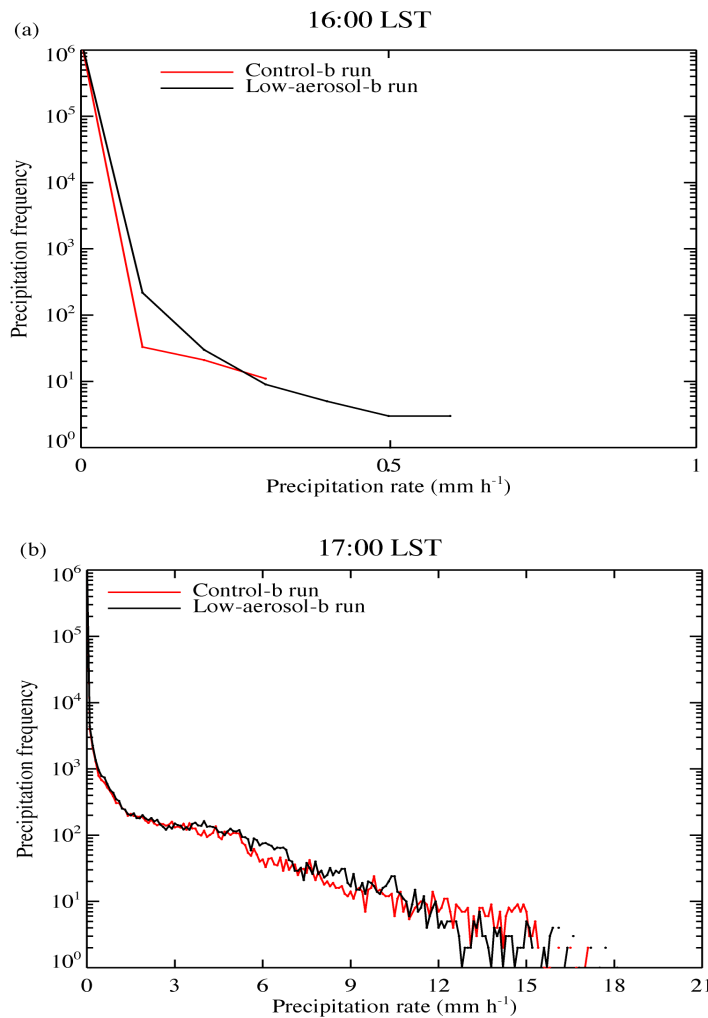
1629

1630  
1631

Figure 8

Deleted: 10

### Beijing case



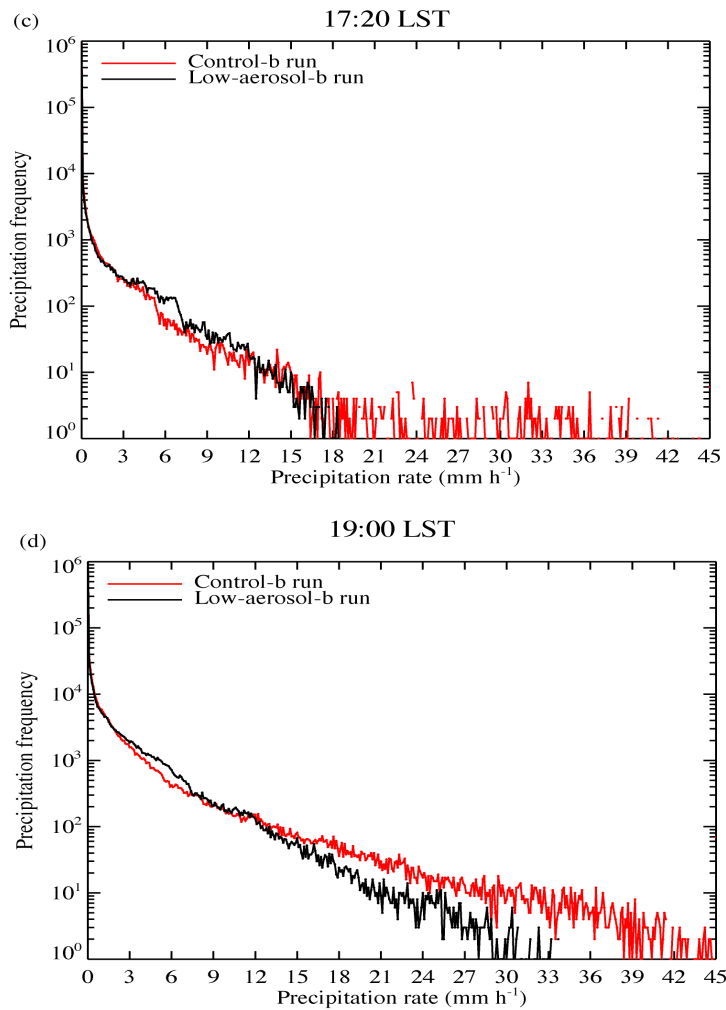
1633

1634

1635

**Figure 9**

Deleted: 11



1637  
1638  
1639  
1640  
1641  
1642

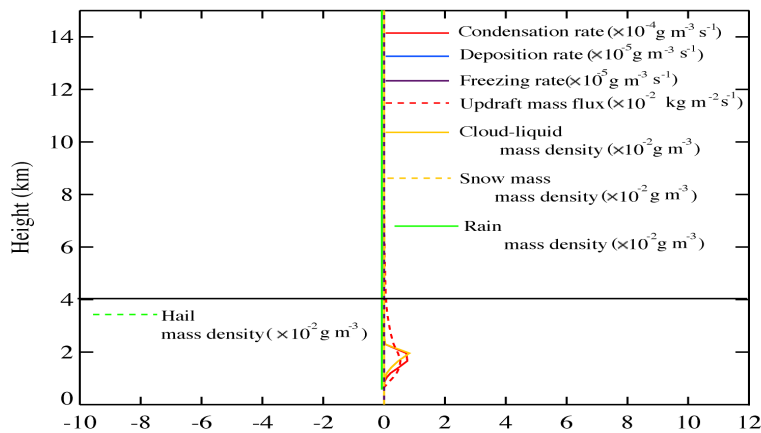
**Figure 9**

Deleted: 11

**Beijing case**  
**(control-b run minus low-aerosol-b run)**

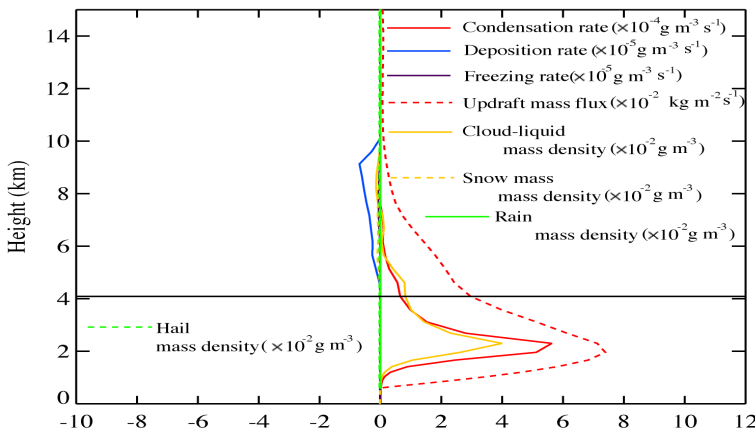
(a)

14:20 LST



(b)

15:40 LST

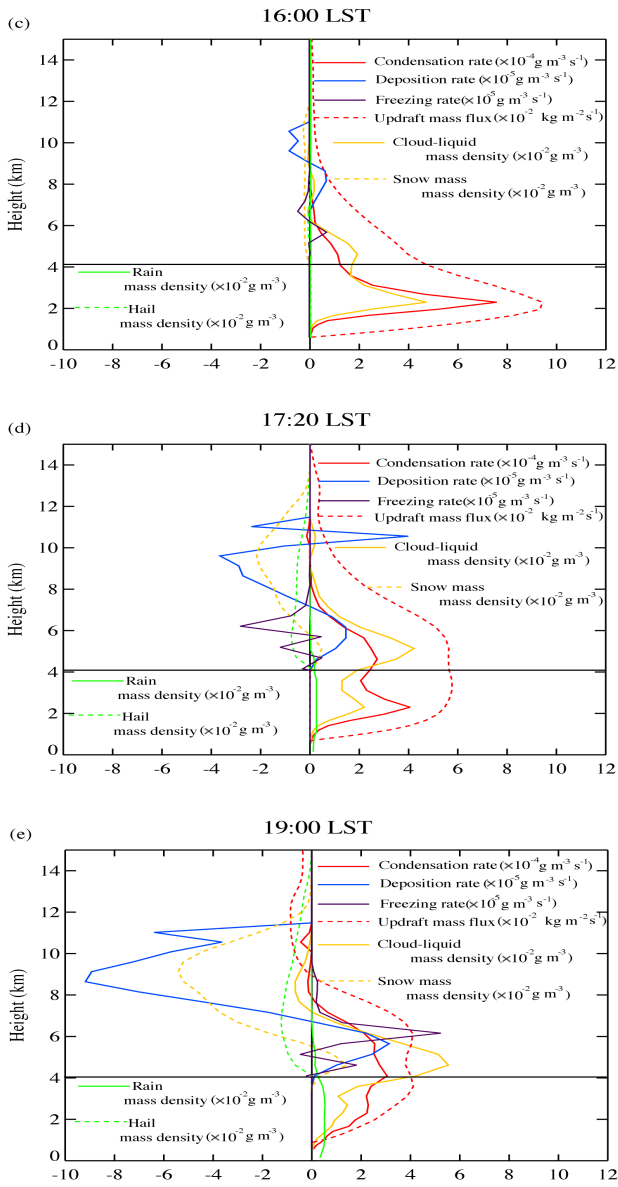


1644

1645

**Figure 10**

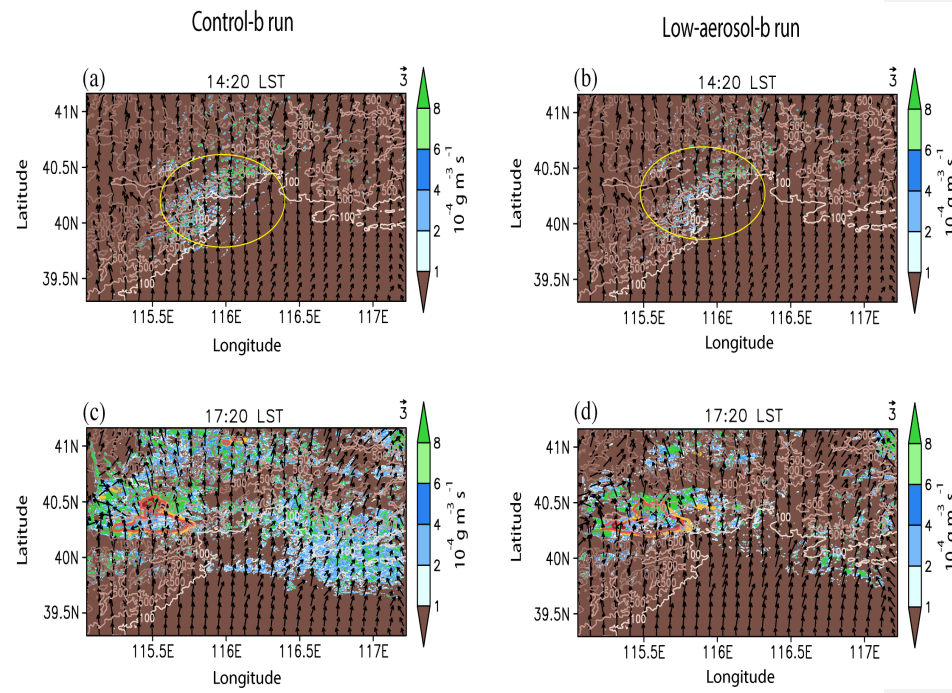
Deleted: 2



1647  
1648

Figure 10

Deleted: 2

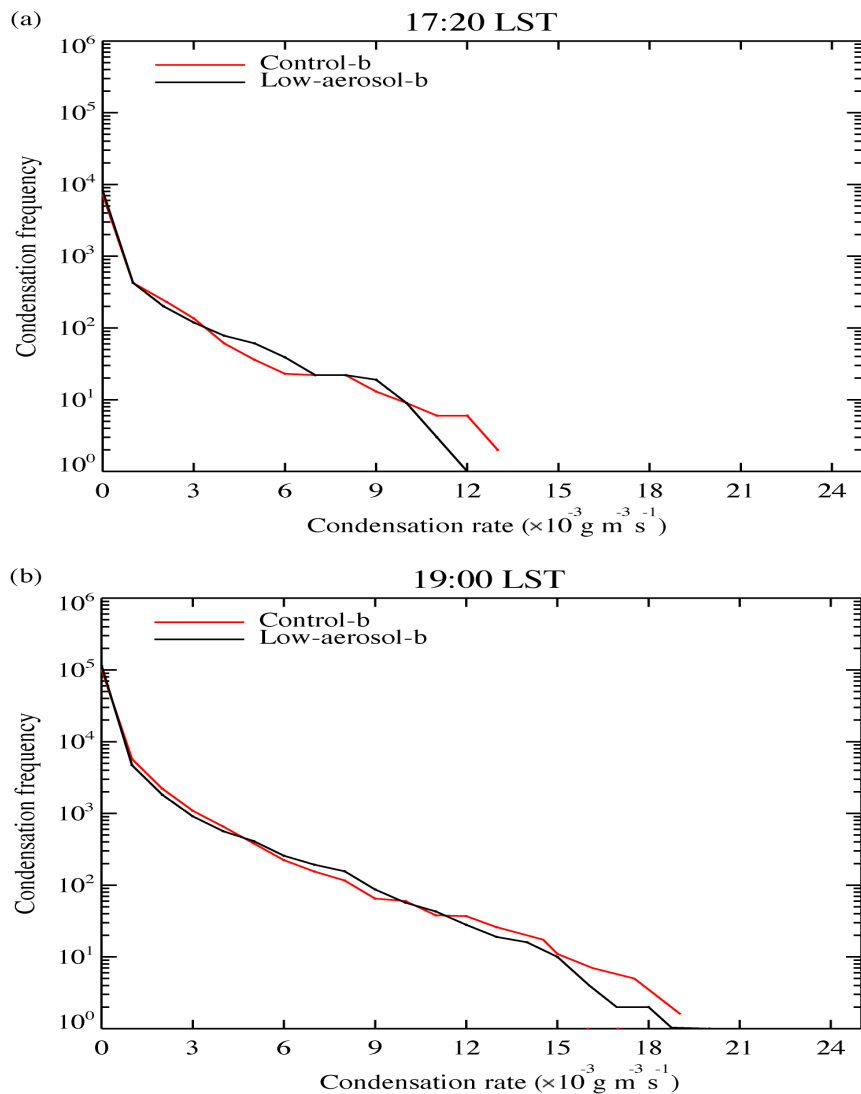


1650  
1651  
1652  
1653  
1654

**Figure 11**

Deleted: 3

### Beijing case

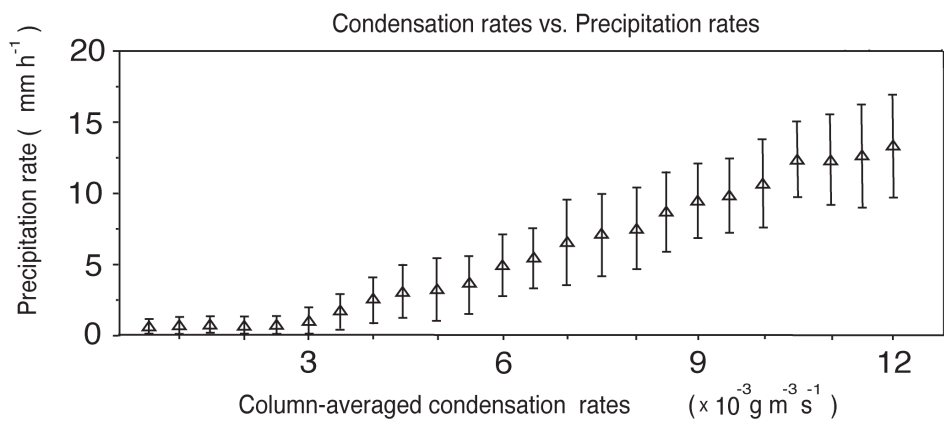


1656

1657

**Figure 12**

Deleted: 4



1659

1660  
1661

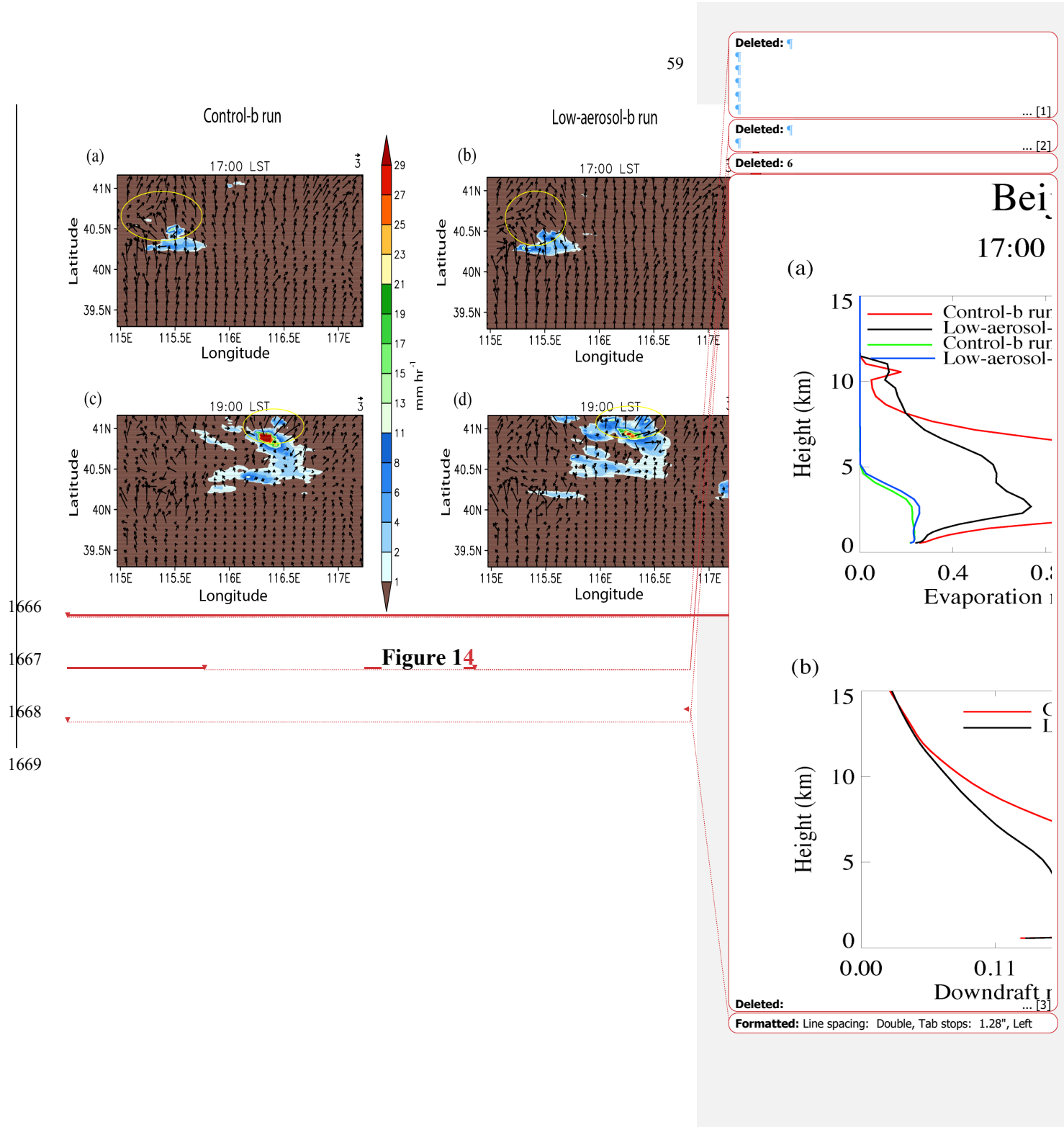
1662

1663

1664

**Figure 13**

Deleted: 5



**Page 59: [1] Deleted**

**Seoung Soo Lee**

**4/18/22 8:24:00 AM**

▼.....  
▲  
**Page 59: [2] Deleted**

**Seoung Soo Lee**

**4/18/22 8:25:00 AM**

▼.....  
▲  
**Page 59: [3] Deleted**

**Seoung Soo Lee**

**4/19/22 3:37:00 PM**

▼.....  
▲